Unmanned Systems, Vol. 14, No. 2 (2026) 281–306

DOI: 10.1142/S2301385025500943

UNMANNED SYSTEMS
https://www.worldscientific.com/worldscinet/us

Modeling, Control and Guidance of an Autonomous Wheeled Mobile Robot AWMR: A Comparative Study between Three Yaw Moment Control Techniques for Autopilot Design with Experimental Results

Helmi Abrougui*, Samir Nejim

Research Laboratory "Marine Technology and Naval Systems"
Naval Academy, Menzel Bourguiba 7050, Tunisia

This paper presents the development of an autopilot system for self-driving an autonomous wheeled vehicle. A mathematical model, including the power allocation system, has been designed for a vehicle with three degrees of freedom. All model parameters have been identified through experimental trials. Heading and speed controllers were designed based on Lyapunov theory. These controllers have been further fine-tuned and tested through simulations to verify their robustness against external disturbances in the system dynamics. Moreover, this work proposes guidance approaches that allow the vehicle to track desired waypoints (line of sight (LOS)), and follow a given path (cross-track error) and a predefined trajectory with obstacle avoidance. A comparative study was also proposed in this paper, wherein we evaluate the paths followed by the vehicle using distinct yaw moment control techniques which are; differential thrust controller, solely relying on a steering controller, and a combination of both. To validate the effectiveness of the proposed autopilot system, we have conducted experimental tests, specifically focusing on waypoint tracking control (LOS method). The results underscore the system's capabilities and its potential in real-world applications.

Keywords: Autonomous wheeled mobile robot; modeling; power allocation; Lyapunov theory; heading and speed controllers; control parameter tuning; yaw moment control techniques; waypoint tracking control; path following control.

1. Introduction

Wheeled mobile robots (WMRs) are a type of nonholonomic system, meaning their motion constraints depend on the direction of movement, which influences how they can follow a given path. To efficiently navigate and maintain stability, these robots can be equipped with various control systems. Over the past 30 years, extensive research has been conducted on the application of advanced front steering (AFS), rear wheel steering (RWS) and four-wheel steering (4WS) systems, particularly in the field of vehicle stability control [21–28]. These systems have proven essential for enhancing vehicle stability by generating a control yaw moment, which is crucial for keeping a vehicle stable during dynamic maneuvers. By adjusting the steering angles of the front, rear, or all wheels, these control systems offer precise management of the vehicle's orientation, helping to counteract external disturbances and ensuring that the WMR remains on its intended path.

The differential controller system for wheeled vehicles [1, 29–31] is another method of steering where the vehicle's direction is controlled by varying the speed of its wheels on either side. This system is commonly used in robots and vehicles with independently driven wheels, such as differential drive robots. One of its key advantages is the exceptional maneuverability it provides, enabling the vehicle to execute tight turns with a small turning radius. This capability is particularly beneficial in environments with limited space, where precise navigation is essential. This makes differential drive systems particularly effective in environments requiring precise navigation.

Received 2 May 2024; Revised 10 December 2024; Accepted 10 December 2024; Published 11 February 2025. This paper was recommended for publication in its revised form by editorial board member, Xuefang Li.
Email Address: *helmi.abrougui@enit.utm.tn*
*Corresponding author.

Controller design for a WMR requires not only the development of a controller to follow a predefined path but also the strong stabilization of the closed loop against introduced disturbances in the system. Linear control technique [22], nonlinear control techniques [7, 8, 12, 13, 16] and artificial intelligence approaches [17, 18] are examples of existent control systems for wheeled vehicles. Adaptive controllers [2], sliding mode control (SMC) [3] and finite-time control approach [4] are also examples of robust and nonlinear controllers.

In order to make the control system more realistic, adaptive compensation is combined in [5] with the above-mentioned control approaches. In addition, a speed controller for a WMR was developed using an adaptative sliding mode approach [6]. In the same context, authors in [7] designed a finite-time approach for tracking control of multiple nonholonomic mobile robots.

An optimal linear quadratic regulator has also been designed in [20] based on the vehicle dynamical model for path tracking. In the same context, the twisting algorithm and the terminal sliding mode (TSM) approach were also designed in [8]. Authors in [9] developed a feedforward controller for designing the heading controller using neural networks. The fuzzy control was used in [10] to improve the performance of classic controllers due to its universal approximation capabilities. In addition, visual servoing tracking controllers were designed in [11].

Based on previous research, the authors have developed both linear and nonlinear control laws to manage a wheeled vehicle, either by steering the front wheels or by controlling the differential thrust force, all grounded on a well-defined mathematical model. To the best of our knowledge, no author has addressed the design of a nonlinear control system considering the three driving modes of wheeled vehicles: differential control, steering angle control and the combination of both. This study aims to compare the performance of these three techniques and propose a generalized mathematical model that can assist researchers in exploiting these control methods and adapting them to their vehicles based on their specific types. Additionally, authors who have developed nonlinear controls, such as sliding mode control, have not rigorously calculated the control gains as proposed in this paper.

This paper aims to overcome these challenges by developing a mathematical model for a wheeled vehicle with three degrees of freedom (3DOF), incorporating the three yaw control techniques. Additionally, it will address the design of an autopilot system for self-driving the vehicle, spanning from theoretical study to experimental results.

The remainder of the paper is structured as follows:

Section 2 deals with the development of a mathematical model, including the power allocation system, with 3DOF describing the behavior of the vehicle in the horizontal plan.

Fig. 1. The considered wheeled vehicle.

The vehicle parameters are identified experimentally in Sec. 3.

In Sec. 4, based on Lyapunov theory, heading and speed controllers are designed and simulation tests are carried out, on the one hand, to validate the designed control laws and to evaluate the yaw moment controller using three different techniques on the other hand.

In Sec. 5, a guidance system is established letting the vehicle to track desired positions, follow a given path and avoid encountered obstacles.

Section 6 is intended to design an autopilot system using an ATmega2560 microcontroller and a graphic processing unit GPU Jetson nano. The developed heading controller is implemented through the microcontroller and the results of the experimental tests are compared with those of the simulation.

The primary contribution of this paper is a comparative study of three yaw moment techniques for heading controller design. Another contribution of this work is the proposed tuning approach for heading controller parameters, which is novel compared to previous studies. In addition, this paper proposes a novel method allowing the vehicle to track a desired position and to follow a given path by the development of a yaw moment controller that recommends the use of a steering angle actuator and a differential thrust at the same time (Fig. 1).

2. System Modeling

2.1. *Reference systems and vehicle description*

Let the (O, X_0, Y_0, Z_0) coordinate system be the inertial reference frame R_0 and let the (G, X, Y, Z) be the body frame R as shown in Fig. 2.

The origin of the body frame coincides with the center of gravity G of the vehicle. The (GX) axis is pointed toward the front of the vehicle, the (GY) one is pointed toward the left side of the vehicle and the (GZ) one is chosen oriented toward the high to have a direct trihedron.

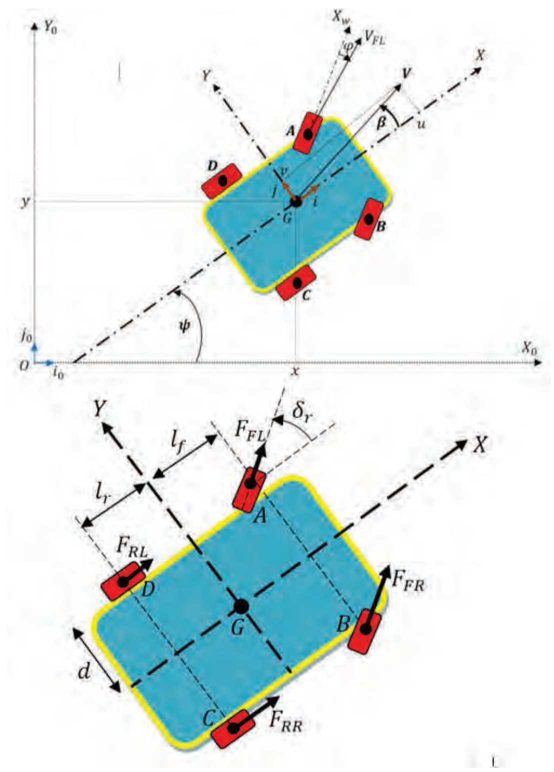

Fig. 2. Geometry model of the considered vehicle.

Let $(\vec{i}, \vec{j}, \vec{k})$ be the unit vectors of the (GX), (GY) and (GZ) axes, respectively.

Let $(\vec{i}_0, \vec{j}_0, \vec{k}_0)$ be the unit vectors of the (OX_0), (OY_0) and (OZ_0) axes, respectively, as shown in Fig. 2.

The considered vehicle is equipped with four identical wheels. They are driven by four identical electric motors.

Each wheel creates a thrust force $\overrightarrow{F}_{\mathrm{FL}}$, $\overrightarrow{F}_{\mathrm{FR}}$, $\overrightarrow{F}_{\mathrm{RL}}$, $\overrightarrow{F}_{\mathrm{RR}}$ applied, respectively, at points A, B, C, D. The vehicle orientation ψ (heading angle) is controlled using three techniques; the steering actuator of the front wheels $\delta_r \in [-\delta_{r_{\max}}, \delta_{r_{\max}}]$, the differential thrust between the left and the right forces or both together at the same time.

The vehicle side slip angle β is the angle between the vehicle longitudinal axis (X-axis) and the velocity vector as shown in Fig. 2. Each wheel has a sideslip angle φ [19] between the wheel longitudinal axis (X_w-axis) and its velocity vector V_{FL}.

2.2. *Assumptions*

The used assumptions for vehicle modeling in this paper are as follows:

- The road surface is horizontal.
- The vehicle is considered a rigid body moving on a flat and horizontal plane (road inclination is equal to zero).
- Only the longitudinal wheel forces are considered, the lateral wheel forces are neglected.
- The resistance model does not depend on the road where the vehicle moves.
- The forces and displacements related to roll, pitch and heave motions are zero. This simplification is based on the assumption that suspension dynamics are neglected and the wheels are considered rigid. As a result, vertical forces, as well as rotational displacements around the vehicle's longitudinal (roll) and lateral (pitch) axes, are not included in the model. This allows us to focus solely on the planar dynamics relevant to vehicle control, while simplifying the model by excluding vertical and rotational movements associated with suspension compliance.

2.3. *Equations of motion*

The notations used in this work are described in Table 1.

The velocity of the vehicle $\vec{V}$ is given by

$$\vec{V} = \begin{pmatrix} u \\ v \\ 0 \end{pmatrix}_R = \begin{pmatrix} \dot{x} \\ \dot{y} \\ 0 \end{pmatrix}_{R_0}. \tag{1}$$

The force applied to the vehicle is expressed in R and R_0 as follows:

$$\vec{F} = \begin{pmatrix} F_x \\ F_y \\ 0 \end{pmatrix}_R = \begin{pmatrix} F_{x_0} \\ F_{y_0} \\ 0 \end{pmatrix}_{R_0}. \tag{2}$$

Table 1. Used notation and description.

Notation	Description
x, y	Horizontal coordinates of G in R_0
ψ	Heading angle
u	Velocity in surge motion
v	Velocity in sway motion
r	Yaw rate
δ_r	Steering angle
$\vec{F}_{\mathrm{FR}}$	Front right wheel force
$\vec{F}_{\mathrm{FL}}$	Front left wheel force
$\vec{F}_{\mathrm{RR}}$	Rear right wheel force
$\vec{F}_{\mathrm{RL}}$	Rear left wheel force
$\vec{f}$	Linear frictional force
l_f	Distance from G to front axle
l_r	Distance from G to rear axle
$\vec{R}$	Turning frictional force
m	Mass of the vehicle
I_z	Moment of inertia of the vehicle around (GZ) axis
d	Distance between G and point A in X–Y plane.
T_s	Sampling time

Points A, B, C, D and G (Fig. 2) are supposed to be located on the same horizontal plane, thus, the moment $\vec{M}$ expressed in R_0 is

$$\vec{M} = \begin{pmatrix} 0 \\ 0 \\ N \end{pmatrix}_{R_0} . \tag{3}$$

By applying the Newton's second law of motion, we obtain

$$\begin{pmatrix} \vec{F} \\ \vec{M} \end{pmatrix} = \begin{pmatrix} m \cdot \vec{a} \\ \vec{\delta} \end{pmatrix} \tag{4}$$

with

$\vec{a} = \frac{d\vec{V}}{dt}$: Linear acceleration,
$\vec{\delta} = \frac{d\vec{\sigma}}{dt}$: Dynamic moment,
$\vec{\sigma} = J\vec{\Omega}$: Angular moment,
J: Inertia matrix of the vehicle,
$\vec{\Omega}$: Angular velocity of the center of gravity G in the inertial frame.

The linear acceleration $\vec{a}$ is thus written as follows:

$$\vec{a} = \ddot{x} \cdot \overrightarrow{i_0} + \ddot{y} \cdot \overrightarrow{j_0} . \tag{5}$$

The angular acceleration is denoted as $\ddot{\psi}$.

Consequently, by using Eq. (4), we get

$$\begin{cases} F_{x_0} = m \cdot \ddot{x}, \\ F_{y_0} = m \cdot \ddot{y}, \\ N = I_z \cdot \ddot{\psi} \end{cases} \tag{6}$$

with I_z the moment of inertia around the (G, Z) axis.

During its movement, the vehicle undergoes a resistance to its movement due to the wind and a frictional force due to the road, this resistance can be represented by a frictional force $\vec{f}$:

$$\vec{f} = -g_1(u)\vec{i} - g_2(v)\vec{j} \tag{7}$$

and a moment $\vec{N}_f$:

$$\vec{N}_f = -g_3(r)\vec{k} \tag{8}$$

with

$g_1(u)$: Surge resistance model,
$g_2(v)$: Sway resistance model,
$g_3(r)$: Yaw resistance model.

We obtain thus

$$\begin{cases} m\ddot{x} = f_{\overrightarrow{i_0}} + F_{\mathrm{FR}_{\overrightarrow{i_0}}} + F_{\mathrm{FL}_{\overrightarrow{i_0}}} + F_{\mathrm{RR}_{\overrightarrow{i_0}}} + F_{\mathrm{RL}_{\overrightarrow{i_0}}}, \\ m\ddot{y} = f_{\overrightarrow{j_0}} + F_{\mathrm{FR}_{\overrightarrow{j_0}}} + F_{\mathrm{FL}_{\overrightarrow{j_0}}} + F_{\mathrm{RR}_{\overrightarrow{j_0}}} + F_{\mathrm{RL}_{\overrightarrow{j_0}}}, \\ I_z\ddot{\psi} = N_{f_{\overrightarrow{k_0}}} + N_{\mathrm{FR}_{\overrightarrow{k_0}}} + N_{\mathrm{FL}_{\overrightarrow{k_0}}} + N_{\mathrm{RR}_{\overrightarrow{k_0}}} + N_{\mathrm{RL}_{\overrightarrow{k_0}}}, \end{cases} \tag{9}$$

where

- $F_{\mathrm{FR}_{\overrightarrow{i_0}}}, F_{\mathrm{FL}_{\overrightarrow{i_0}}}, F_{\mathrm{RR}_{\overrightarrow{i_0}}}, F_{\mathrm{RL}_{\overrightarrow{i_0}}}$ are the components of $\overrightarrow{F_{\mathrm{FR}}}$, $\overrightarrow{F_{\mathrm{FL}}}$, $\overrightarrow{F_{\mathrm{RR}}}$ and $\overrightarrow{F_{\mathrm{RL}}}$, respectively, along (OX_0) axis,
- $F_{\mathrm{FR}_{\overrightarrow{j_0}}}, F_{\mathrm{FL}_{\overrightarrow{j_0}}}, F_{\mathrm{RR}_{\overrightarrow{j_0}}}, F_{\mathrm{RL}_{\overrightarrow{j_0}}}$ are the components of $\overrightarrow{F_{\mathrm{FR}}}$, $\overrightarrow{F_{\mathrm{FL}}}$, $\overrightarrow{F_{\mathrm{RR}}}$ and $\overrightarrow{F_{\mathrm{RL}}}$, respectively, along (OY_0) axis,
- $f_{\overrightarrow{i_0}}, f_{\overrightarrow{j_0}}$ are the components of the frictional force $\vec{f}$ along (OX_0) and (OY_0) axes, respectively,
- $N_{\mathrm{FR}_{\overrightarrow{k_0}}}, N_{\mathrm{FL}_{\overrightarrow{k_0}}}, N_{\mathrm{RR}_{\overrightarrow{k_0}}}, N_{\mathrm{RL}_{\overrightarrow{k_0}}}$ are the moments created by the forces $\overrightarrow{F_{\mathrm{FR}}}$, $\overrightarrow{F_{\mathrm{FL}}}$, $\overrightarrow{F_{\mathrm{RR}}}$ and $\overrightarrow{F_{\mathrm{RL}}}$ around the (OZ_0) axis,
- $N_{f_{\overrightarrow{k_0}}}$ is the component of the moment $\overrightarrow{N_f}$ around the (OZ_0) axis.

In the body frame, we have

$$\vec{F}_{\mathrm{FR}} = \begin{pmatrix} F_{\mathrm{FR}} \cos(\delta_r) \\ F_{\mathrm{FR}} \sin(\delta_r) \\ 0 \end{pmatrix}_R , \tag{10}$$

$$\vec{F}_{\mathrm{FL}} = \begin{pmatrix} F_{\mathrm{FL}} \cos(\delta_r) \\ F_{\mathrm{FL}} \sin(\delta_r) \\ 0 \end{pmatrix}_R , \tag{11}$$

$$\vec{F}_{\mathrm{RR}} = \begin{pmatrix} F_{\mathrm{RR}} \\ 0 \\ 0 \end{pmatrix}_R , \tag{12}$$

$$\vec{F}_{\mathrm{RL}} = \begin{pmatrix} F_{\mathrm{RL}} \\ 0 \\ 0 \end{pmatrix}_R , \tag{13}$$

$$\vec{f} = \begin{pmatrix} -g_1(u) \\ -g_2(v) \\ 0 \end{pmatrix}_R . \tag{14}$$

By using the following transformation matrix

$$P_{R_0 \to R} = \begin{pmatrix} \cos\psi & \sin\psi & 0 \\ -\sin\psi & \cos\psi & 0 \\ 0 & 0 & 1 \end{pmatrix}, \tag{15}$$

we get

$$\vec{F}_{\mathrm{FR}} = \begin{pmatrix} F_{\mathrm{FR}} \cos(\delta_r + \psi) \\ F_{\mathrm{FR}} \sin(\delta_r + \psi) \\ 0 \end{pmatrix}_{R_0} , \tag{16}$$

$$\vec{F}_{\mathrm{FL}} = \begin{pmatrix} F_{\mathrm{FL}} \cos(\delta_r + \psi) \\ F_{\mathrm{FL}} \sin(\delta_r + \psi) \\ 0 \end{pmatrix}_{R_0} , \tag{17}$$

$$\vec{F}_{\mathrm{RR}} = \begin{pmatrix} F_{\mathrm{RR}} \cos(\psi) \\ F_{\mathrm{RR}} \sin(\psi) \\ 0 \end{pmatrix}_{R_0} , \tag{18}$$

$$\vec{F}_{\mathrm{RL}} = \begin{pmatrix} F_{\mathrm{RL}} \cos(\psi) \\ F_{\mathrm{RL}} \sin(\psi) \\ 0 \end{pmatrix}_{R_0}, \tag{19}$$

$$\vec{f} = \begin{pmatrix} -g_1(u)\cos(\psi) - g_2(v)\sin(\psi) \\ -g_1(u)\sin(\psi) - g_2(v)\cos(\psi) \\ 0 \end{pmatrix}_{R_0}. \tag{20}$$

- Moment $\vec{N}_{\mathrm{FL}}$ is calculated as follows:

$$\vec{N}_{\mathrm{FL}} = \vec{F}_{\mathrm{FL}} \wedge \vec{AG} \tag{21}$$

with

$$\vec{AG} = \begin{pmatrix} -l_f \\ -d \\ 0 \end{pmatrix}_R = \begin{pmatrix} d\sin(\psi) - l_f\cos(\psi) \\ -l_f\sin(\psi) - d\cos(\psi) \\ 0 \end{pmatrix}_{R_0}. \tag{22}$$

Moment $\vec{N}_{\mathrm{FL}}$ becomes

$$\vec{N}_{\mathrm{FL}} = F_{\mathrm{FL}}(l_f \sin(\delta_r) - d\cos(\delta_r))\vec{k}_0. \tag{23}$$

By replacing $-d$ with d in Eq. (23) we get the moment $\vec{N}_{\mathrm{FR}}$ as follows:

$$\vec{N}_{FR} = F_{\mathrm{FR}} \cdot (l_f \sin(\delta_r) + d\cos(\delta_r)) \cdot \vec{k_0}. \tag{24}$$

Moment $\vec{N}_{\mathrm{RR}}$ is calculated as follows:

$$\vec{N}_{\mathrm{RR}} = \vec{F}_{\mathrm{RR}} \wedge \vec{CG} \tag{25}$$

wit

$$\vec{CG} = \begin{pmatrix} l_r \\ d \\ 0 \end{pmatrix}_R = \begin{pmatrix} -d\sin(\psi) + l_r\cos(\psi) \\ l_r\sin(\psi) + d\cos(\psi) \\ 0 \end{pmatrix}_{R_0}. \tag{26}$$

Moment $\vec{N}_{\mathrm{RR}}$ becomes

$$\vec{N}_{\mathrm{RR}} = dF_{\mathrm{RR}}\vec{k_0}. \tag{27}$$

By replacing $-d$ with d in Eq. (27), the moment $\vec{N}_{\mathrm{RL}}$ is given as follows:

$$\vec{N}_{\mathrm{RL}} = -dF_{\mathrm{RL}}\vec{k}_0. \tag{28}$$

Consequently, we get

$$\begin{cases} m\ddot{x} = (F_{\mathrm{FL}} + F_{\mathrm{FR}})\cos(\delta_r + \psi) + (F_{\mathrm{RL}} + F_{\mathrm{RR}})\cos(\psi) \\ \qquad -g_1(u)\cos(\psi) - g_2(v)\sin(\psi), \\ m\ddot{y} = (F_{\mathrm{FL}} + F_{\mathrm{FR}})\sin(\delta_r + \psi) + (F_{\mathrm{RL}} + F_{\mathrm{RR}})\sin(\psi) \\ \qquad -g_1(u)\sin(\psi) - g_2(v)\cos(\psi), \\ I_z \cdot \ddot{\psi} = (F_{\mathrm{FR}} + F_{\mathrm{FL}})l_f\sin(\delta_r) + d(F_{\mathrm{FR}} - F_{\mathrm{FL}})\cos(\delta_r) \\ \qquad + d(F_{\mathrm{RR}} - F_{\mathrm{RL}}) - g_3(r) \end{cases} \tag{29}$$

with $r = \dot{\psi}$.

By normalizing, it means dividing by the maximum force $F_{\max}$, which can be generated by each motor, Eqs. (29) become

$$\begin{cases} \dfrac{m\ddot{x}}{F_{\max}} = \dfrac{(F_{\mathrm{FL}} + F_{\mathrm{FR}})\cos(\delta_r + \psi) + (F_{\mathrm{RL}} + F_{\mathrm{RR}})\cos(\psi)}{F_{\max}} \\ \qquad \times \dfrac{-g_1(u)\cos(\psi) - g_2(v)\sin(\psi)}{F_{\max}}, \\ \dfrac{m\ddot{y}}{F_{\max}} = \dfrac{(F_{\mathrm{FL}} + F_{\mathrm{FR}})\sin(\delta_r + \psi) + (F_{\mathrm{RL}} + F_{\mathrm{RR}})\sin(\psi)}{F_{\max}} \\ \qquad \times \dfrac{-g_1(u)\sin(\psi) - g_2(v)\cos(\psi)}{F_{\max}}, \\ \dfrac{I_z \cdot \ddot{\psi}}{F_{\max}} = \dfrac{(F_{\mathrm{FR}} + F_{\mathrm{FL}})l_f\sin(\delta_r) + d(F_{\mathrm{FR}} - F_{\mathrm{FL}})\cos(\delta_r)}{F_{\max}} \\ \qquad \times \dfrac{+d(F_{\mathrm{RR}} - F_{\mathrm{RL}}) - g_3(r)}{F_{\max}}. \end{cases} \tag{30}$$

Let us pose

- $m' = \frac{m}{F_{\max}}$,
- $I'_z = \frac{I_z}{F_{\max}}$,
- $F'_{\mathrm{FL}} = \frac{F_{\mathrm{FL}}}{F_{\max}}, F'_{\mathrm{FR}} = \frac{F_{\mathrm{FR}}}{F_{\max}}, F'_{\mathrm{RL}} = \frac{F_{\mathrm{RL}}}{F_{\max}}, F'_{\mathrm{RR}} = \frac{F_{\mathrm{RR}}}{F_{\max}}$.

We get

$$\begin{cases} m'\ddot{x} = (F'_{\mathrm{FL}} + F'_{\mathrm{FR}})\cos(\delta_r + \psi) + (F'_{\mathrm{RL}} + F'_{\mathrm{RR}})\cos(\psi) \\ \qquad - g_1(u)\cos(\psi) - g_2(v)\sin(\psi), \\ m'\ddot{y} = (F'_{\mathrm{FL}} + F'_{\mathrm{FR}})\sin(\delta_r + \psi) + (F'_{\mathrm{RL}} + F'_{\mathrm{RR}})\sin(\psi) \\ \qquad - g_1(u)\sin(\psi) - g_2(v)\cos(\psi), \\ I'_z \cdot \ddot{\psi} = (F'_{\mathrm{FL}} + F'_{\mathrm{FR}})l_f\sin(\delta_r) + d(F'_{FL} - F'_{FR})\cos(\delta_r) \\ \qquad + d(F'_{\mathrm{RR}} + F'_{\mathrm{RL}}) - g_3(r). \end{cases} \tag{31}$$

Since we have

$$\vec{V} = \dot{x} \cdot \overrightarrow{i_0} + \dot{y} \cdot \overrightarrow{j_0} = u \cdot \vec{i} + v \cdot \vec{j} \tag{32}$$

and

$$\begin{cases} \vec{i}_0 = \cos\psi \cdot \vec{i} - \sin\psi \cdot \vec{j}, \\ \vec{j}_0 = \sin\psi \cdot \vec{i} + cos\psi \cdot \vec{j}, \end{cases} \tag{33}$$

we get

$$\begin{cases} u = \dot{x}\cos\psi + \dot{y}\sin\psi, \\ v = -\dot{x}\sin\psi + \dot{y}\cos\psi. \end{cases} \tag{34}$$

Time derivative of Eqs. (34) gives

$$\begin{cases} \dot{u} = \ddot{x}\cos\psi - \dot{x}.\dot{\psi} \cdot \sin\psi + \ddot{y} \cdot \sin\psi + \dot{\psi} \cdot \dot{y} \cdot \cos\psi, \\ \dot{v} = -\ddot{x}\sin\psi - \dot{x} \cdot \dot{\psi} \cdot \cos\psi + \ddot{y} \cdot \cos\psi - \dot{\psi} \cdot \dot{y} \cdot \sin\psi. \end{cases} \tag{35}$$

It is equivalent to

$$\begin{cases} m'.\dot{u} = m'\ddot{x}\cos\psi - m'\dot{x}.\dot{\psi}.\sin\psi \\ +m'\ddot{y}.\sin\psi + m'\dot{\psi}.\dot{y}.\cos\psi, \\ m'.\dot{v} = -m'.\ddot{x}\sin\psi - m'.\dot{x}.\dot{\psi}.\cos\psi \\ +m'.\ddot{y}.\cos\psi - m'\dot{\psi}.\dot{y}.\sin\psi. \end{cases} \tag{36}$$

So, we get

$$\dot{u} = \frac{(F'_{\mathrm{FL}} + F'_{\mathrm{FR}})cos(\delta_r) + (F'_{\mathrm{RL}} + F'_{\mathrm{RR}}) + m'rv - g_1(u)}{m'}, \tag{37}$$

$$\dot{v} = \frac{(F'_{\mathrm{FL}} + F'_{\mathrm{FR}})\sin(\delta_r) - m'ru - g_2(v)}{m'}. \tag{38}$$

The dynamic model of the vehicle is thus given by the following differential equations:

$$\begin{cases} \dot{x} = u\cos\psi - v\sin\psi, \\ \dot{y} = u\sin\psi + v\cos\psi, \\ \dot{\psi} = r, \\ \dot{u} = \dfrac{(F'_{\mathrm{FL}} + F'_{\mathrm{FR}})\cos(\delta_r) + (F'_{\mathrm{RL}} + F'_{\mathrm{RR}}) + m'rv - g_1(u)}{m'}, \\ \dot{v} = \dfrac{(F'_{\mathrm{FL}} + F'_{\mathrm{FR}})\sin(\delta_r) - m'ru - g_2(v)}{m'}, \\ \dot{r} = \dfrac{l_f\sin(\delta_r)(F'_{\mathrm{FL}} + F'_{\mathrm{FR}}) + d\cos(\delta_r)(F'_{\mathrm{FR}} - F'_{\mathrm{FL}}) + d(F'_{\mathrm{FR}} - F'_{\mathrm{FL}}) - g_3(r)}{I'_z}. \end{cases} \tag{39}$$

When turning for example to the left side, the angular velocity of the left wheels is less than the angular velocity of the right wheels. Therefore, let us pose $F'_{\mathrm{FL}} = F'_{\mathrm{RL}} = F'_L$ and $F'_{\mathrm{FR}} = F'_{\mathrm{RR}} = F'_R$.

So, we get

$$\begin{cases} \dot{x} = u\cos\psi - v\sin\psi, \\ \dot{y} = u\sin\psi + v\cos\psi, \\ \dot{\psi} = r, \\ \dot{u} = \dfrac{\tau_{\mathrm{speed}} + m'rv - g_1(u)}{m'}, \\ \dot{v} = \dfrac{\frac{\tau_{\mathrm{steering}}}{l_f} - m'ru - g_2(v)}{m'}, \\ \dot{r} = \dfrac{\tau_{\mathrm{steering}} + \tau_{\mathrm{diff}} - g_3(r)}{I'_z} \end{cases} \tag{40}$$

with

$$\begin{aligned} \tau_{\mathrm{speed}} &= (F'_L + F'_R)(\cos(\delta_r) + 1), \\ \tau_{\mathrm{steering}} &= l_f(F'_L + F'_R)\sin(\delta_r), \\ \tau_{\mathrm{diff}} &= d(F'_R - F'_L)(\cos(\delta_r) + 1), \end{aligned} \tag{41}$$

τ_{speed} is the thrust force that controls the vehicle speed, τ_{steering} is the yaw moment that controls the vehicle orientation by using only the steer system and τ_{diff} is the yaw moment control due only to the differential thrust between forces F'_R and F'_L. We can define thus the total yaw moment control by

$$\tau_{\mathrm{turn}} = \tau_{\mathrm{steering}} + \tau_{\mathrm{diff}}.$$

The developed model is nonlinear. It has the form $\dot{X} = f(X, U)$, where $X = (x\, y\, \psi\, u\, v\, r)^T$ is the state vector and the selected input vector is $U = (\tau_{\mathrm{speed}}\ \tau_{\mathrm{turn}})^T$.

From Eqs. (41), $\sin(\delta_r)$ and $\cos(\delta_r)$ can be approximated with first-order Taylor polynomials ($\sin(\delta_r) = \delta_r$ and $\cos(\delta_r) = 1$); with the assumption that the steering angle δ_r is limited to a value which is less than 20°. (This is a mechanical constraint in the actual vehicle model, which prevents the front wheel steering angle from exceeding 20°.)

We can thus design the power allocation system as follows:

$$\begin{aligned} F'_L &= \frac{\tau_{\mathrm{speed}}}{4} + \frac{\tau_{\mathrm{turn}}}{8d}, \\ F'_R &= \frac{\tau_{\mathrm{speed}}}{4} - \frac{\tau_{\mathrm{turn}}}{8d}, \\ \delta_r &= \frac{\tau_{\mathrm{turn}}}{d\tau_{\mathrm{speed}}}, \end{aligned} \tag{42}$$

Therefore, the power allocation scheme is described in Fig. 3.

The steering angle δ_r is controlled by a servomotor. Its angular velocity $\dot{\delta}_r$ is thus saturated $|\dot{\delta}_r| < \dot{\delta}_{r_{\max}}$.

The steering angle actuator can be modeled by a first-order low-pass filter with time constant T (see Fig. 4). The transfer function of the filter is

$$H_1(s) = \frac{1}{1 + Ts}. \tag{43}$$

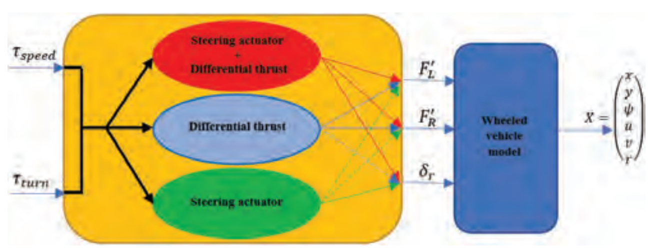

Fig. 3. Power allocation scheme.

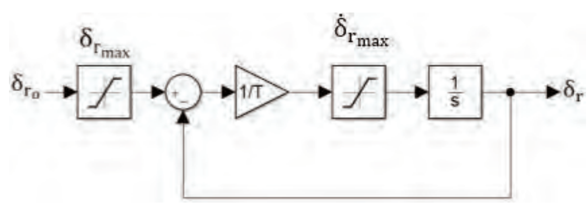

Fig. 4. Steering angle actuator model.

We get so

$$\dot{\delta}_r = \operatorname{sat}\left(\frac{1}{T}(\operatorname{sat}(\delta_{r_o}, \delta_{r_{\max}}) - \delta_r), \dot{\delta}_{r_{\max}}\right), \tag{44}$$

where δ_{r_o} is the ordered steering angle.

In the following section, we propose a new approach for parameter identification of the vehicle-developed model, which are m', I'_z, $g_1(u)$, $g_2(v)$, $g_3(r)$.

3. Parameter Identification

3.1. *Determination of the surge resistance model $g_1(u)$*

The resistance model $g_1(u)$ in surge motion can be determined using linear uniform motion. This motion is obtained by applying at each time a constant pushing force while keeping the steering angle $\delta_r = 0$. It leads to a steady state characterized by a constant speed in surge $\dot{u} = 0$ and $r = 0$.

This approach involves measuring the elapsed time Δt taking by the vehicle to travel a known distance $D = 10$ during the steady state.

Accordingly, we have

$$\dot{u} = \frac{\tau_{\text{speed}} - g_1(u)}{m'} = 0, \tag{45}$$

meaning that

$$\tau_{\text{speed}} = g_1(u). \tag{46}$$

All data corresponding to this trial are presented in Table 2.

By plotting $\tau_{\text{speed}} = g_1(u)$, we get the red points shown in Fig. 5.

The resistance model of the linear motion can be thus approximated by $g_1(u) = \alpha_1 u^{\beta_1}$ (the curve is presented with blue color in Fig. 5). With $\alpha_1 > 0$ and $\beta_1 \in]0, 1]$ that will be calculated using the Least mean square (LMS) method [14, 15] as follows.

We have

$$\tau_{\text{speed}} = g_1(u) = \alpha_1 u^{\beta_1}. \tag{47}$$

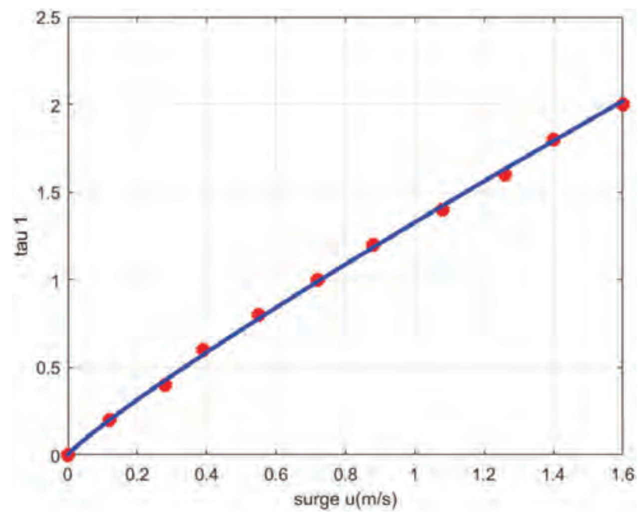

Fig. 5. Damping model of the linear motion.

Therefore,

$$\log(\tau_{\text{speed}}) = \log(\alpha_1) + \beta_1 \log(u). \tag{48}$$

Based on the experimental results presented in Table 2, we obtain

$$\begin{bmatrix} \log(\tau_{\text{speed}_0}) \\ \cdot \\ \cdot \\ \cdot \\ \log(\tau_{\text{speed}_{11}}) \end{bmatrix} = \begin{bmatrix} 1 & \log(u_0) \\ \cdot & \cdot \\ \cdot & \cdot \\ \cdot & \cdot \\ 1 & \log(u_{11}) \end{bmatrix} \begin{bmatrix} \log(\alpha_1) \\ \beta_1 \end{bmatrix}. \tag{49}$$

Equation (49) is written in the following form:

$$Z = P \cdot \theta \tag{50}$$

with

$$Z = \begin{bmatrix} \log(\tau_{\text{speed}_0}) \\ \cdot \\ \cdot \\ \cdot \\ \log(\tau_{\text{speed}_{11}}) \end{bmatrix}, \tag{51}$$

Table 2. Experimental data corresponding to linear uniform motion trial.

	Trial 1	Trial 2	Trial 3	Trial 4	Trial 5	Trial 6
τ_{speed}	0	0.2	0.4	0.6	0.8	1
$\Delta t(\text{s})$	0	79.16	35.3	25.5	18	13.9
$u(\text{ms}^{-1})$	0	0.12	0.28	0.39	0.55	0.72
	Trial 7	Trial 8	Trial 9	Trial 10	Trial 11	
τ_{speed}	1.2	1.4	1.6	1.8	2	
$\Delta t(\text{s})$	11.3	9.26	7.9	6.7	6	
$u(\text{ms}^{-1})$	0.88	1.03	1.26	1.49	$u_{\max} = 1.66$	

$$P = \begin{bmatrix} 1 & \log(u_0) \\ \cdot & \cdot \\ \cdot & \cdot \\ \cdot & \cdot \\ 1 & \log(u_{11}) \end{bmatrix}, \quad (52)$$

$$\theta = \begin{bmatrix} \log(\alpha_1) \\ \beta_1 \end{bmatrix}. \quad (53)$$

Therefore θ can be approximated by the following relation:

$$\hat{\theta} = (P^T P)^{-1} P^T Z. \quad (54)$$

3.2. *Calculation of the coefficient m'*

m' can be determined by applying the following steps:

- Apply maximum traction force to the vehicle in linear motion ($\tau_{\text{speed}} = 2, \delta_r = 0$).
- At $t = 0$, by stopping all motors, we get ($u = u_{\max}$) and ($\tau_{\text{speed}} = 0$).
- Record the elapsed time t_a for stopping ($u = 0$).

m' will therefore be determined as follows.

Using the following equation

$$\dot{u} = \frac{-\alpha_1 u^{\beta_1}}{m'}, \quad (55)$$

we get

$$\frac{du}{dt} = \frac{-\alpha_1 u^{\beta_1}}{m'}. \quad (56)$$

It means that

$$\frac{du}{u^{\beta_1}} = \frac{-\alpha_1}{m'} dt. \quad (57)$$

Integrating Eq. (57), we get

$$\left[\frac{1}{1-\beta_1} u^{1-\beta_1}\right]_{u_{\max}}^{0} = \frac{-\alpha_1}{m'} [t]_0^{t_a}, \quad (58)$$

$$\frac{1}{1-\beta_1} u_{\max}^{1-\beta_1} = \frac{\alpha_1}{m'} t_a. \quad (59)$$

Consequently, we get

$$m' = \frac{(1-\beta_1)\alpha_1 t_a}{u_{\max}^{1-\beta_1}}. \quad (60)$$

3.3. *Determination of the yaw resistance model $g_3(r)$*

This trial consists in turning the vehicle with a uniform yaw motion $\dot{r} = 0$:

- The thrust force is chosen to be constant $F'_R = F'_L = F' = 35\%$.
- $\tau_{\text{turn}} = \tau_{\text{steering}}$

$$= 2 l_f F' \sin(\delta_r).$$

The turn motion is obtained by setting each time a constant steering angle δ_r turning the vehicle with a constant yaw rate r that is measured by counting the elapsed time needed to accomplish a complete turn (360°).

The angular acceleration $\dot{r}$ is given by

$$\dot{r} = \frac{2 l_f F' \sin(\delta_r) - g_3(r)}{I'_z}. \quad (61)$$

However, when the steady state is reached, the yaw rate r is constant and its time derivative $\dot{r}$ is equal to zero.

So,

$$\tau_{\text{turn}} = 2 l_f F' \sin(\delta_r) = g_3(r). \quad (62)$$

All data corresponding to this trial are presented in Table 3.

The curve (see Fig. 6) represents the yaw moment τ_{turn} as a function of the angular speed r. Points in green color are the results of the experimental tests presented in Table 3. The curve in pink color represents an approximation of the yaw resistance model.

Table 3. Experimental data corresponding to turning trial.

	Thrust force $F' = 0.35$				
δ_r (°)	5	10	15	20	25
Elapsed time Δt (s)	83.34	71	41.54	29.37	23.9
r (rad/s)	0.038	0.088	0.15	0.22	0.265
τ_{turn} (N · m)	0.02	0.042	0.064	0.086	0.1

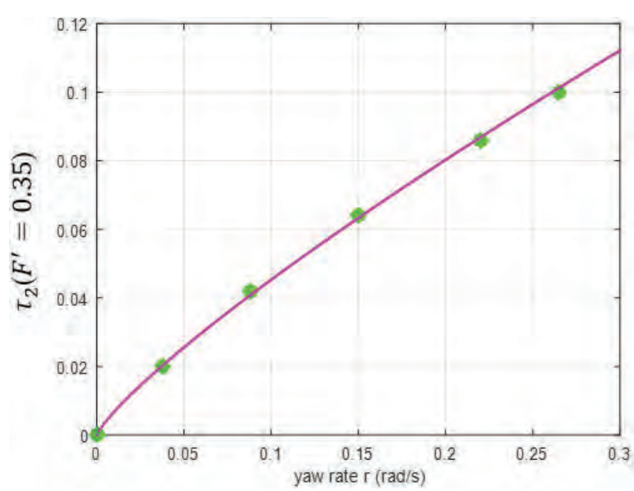

Fig. 6. Resistance model of the turn motion.

The turning resistance model can be therefore approximated by

$$g_3(r) = \alpha_3 r^{\beta_3}, \tag{63}$$

where α_3 and β_3 are calculated using the method described in the previous section.

3.4. *Calculation of the inertia moment I'_z*

The formula currently used for calculating the moment of inertia in yaw is that of a rectangular box which assumes uniform mass distribution (Fig. 7). Because pitch and roll dynamics is ignored in the simulator, the moment of inertia around these axes I_x and I_y were not measured.

Length $b = 1.32\,\text{m}$,
Width $a = 0.78\,\text{m}$,
Height $c = 0.53\,\text{m}$,
Mass $m = 37\,\text{kg}$.

The inertia matrix J of the rectangular parallelepiped is written as follows:

$$J = \begin{bmatrix} I_x & 0 & 0 \\ 0 & I_y & 0 \\ 0 & 0 & I_z \end{bmatrix}_R \tag{64}$$

with

$$I_z = \frac{m(a^2 + b^2)}{12}. \tag{65}$$

Since we have

$$m' = \frac{m}{F_{\max}} \tag{66}$$

and

$$I'_z = \frac{I_z}{F_{\max}}, \tag{67}$$

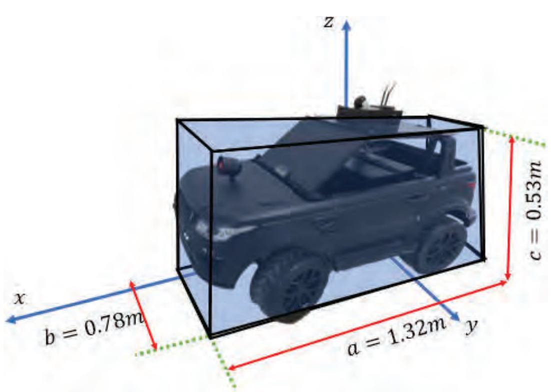

Fig. 7. Homogeneous rectangular parallelepiped.

we get

$$I'_z = \frac{m'}{m} I_z. \tag{68}$$

3.5. *Model validation*

3.5.1. *First trial: Linear motion*

The trial based on linear motion involves applying the maximum thrust force $\tau_{\text{speed}} = 2$ with a yaw moment τ_{turn} equal to zero. Once linear uniform motion is achieved, the steady-state value of the vehicle's speed is $u_{\max}$, as illustrated in Fig. 8.

3.5.2. *Second trial: Turning motion*

The trial based on turning motion consists in applying to the vehicle a constant thrust force τ_{speed} and a constant yaw moment $\tau_{\text{turn}} = 0.4$. The vehicle turns and its trajectory tends to a circle in steady state as presented in the simulation result (Fig. 9).

We note that the turning diameter, in case of using the combined yaw moment controller τ_{turn}, is more or less than the two other techniques τ_{diff} and τ_{steering}.

In this section, we identified the resistance model for linear and turning motions of the considered wheeled vehicle. Then a numerical simulator was developed to validate the mathematical model of the vehicle.

In the next section and based on the developed model, control and guidance approaches will be designed for self-driving the vehicle.

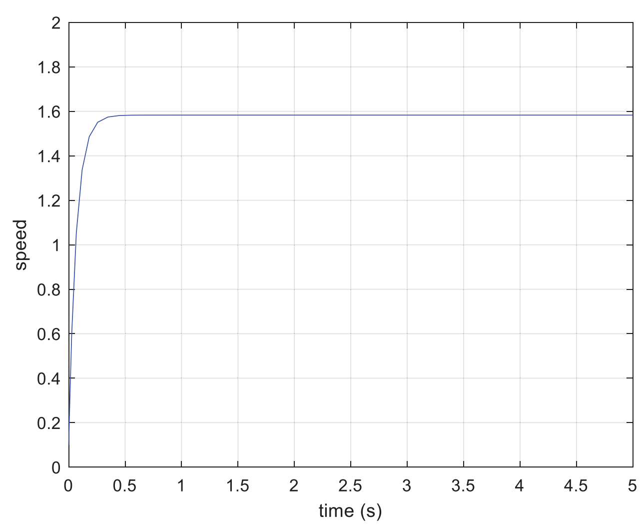

Fig. 8. Surge speed (m/s) in uniform linear motion.

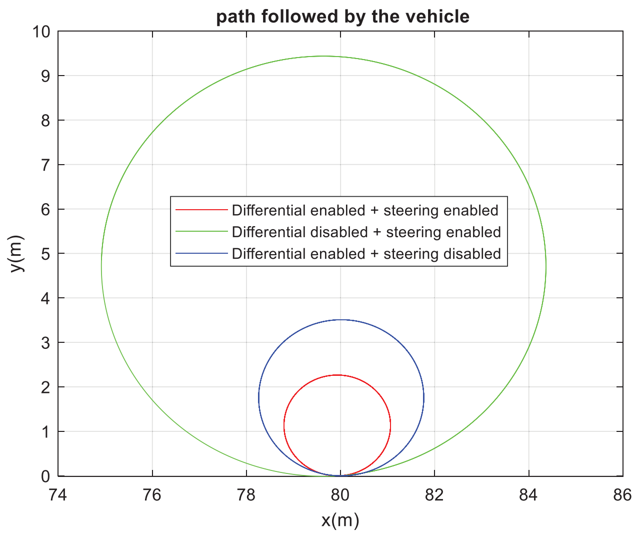

Fig. 9. Trajectory followed by the vehicle.

4. System Control

Theorem 4.1 *An autonomous system* $\dot{x} = f(x)$ *has an equilibrium point* $x_e = 0$ *that is in turn globally and asymptotically stable if there is a continuous scalar function* $V(x)$ *having the following properties:*

$$\begin{cases} V(0) = 0, \\ V(x) > 0 \quad \forall x \neq 0, \\ \lim\limits_{x \to +\infty} V(x) = +\infty, \\ \dot{V}(x) < 0 \quad \forall x \neq 0. \end{cases} \tag{69}$$

Proof. Let us consider a system written in the following form:

$$\begin{cases} \dot{x}_1 = f_1(x_1) + g_1(x_1)x_2, \\ \dot{x}_2 = f_2(x_1, x_2) + g_2(x_1, x_2)u(t), \end{cases} \tag{70}$$

where f_i and $g_i (i = 1, 2)$ are nonlinear functions, $u(t)$ is the input control. $u(t)$ should be calculated letting x_1 to converge to a setpoint x_{1d}.

Let us define the error of the first variable x_1 by

$$e = x_{1d} - x_1. \tag{71}$$

And the sliding surface S is

$$S = \dot{e} + \lambda e, \tag{72}$$

λ is a positive design parameter.

Let us define the Lyapunov candidate function as follows:

$$V = \frac{1}{2}S^2. \tag{73}$$

The time derivative of V is

$$\begin{aligned} \dot{V} &= S\dot{S} \\ &= (\ddot{e} + \lambda\dot{e})S \\ &= (\ddot{x}_{1d} - \ddot{x}_1 + \lambda\dot{e})S \end{aligned} \tag{74}$$

with

$$\begin{aligned} \ddot{x}_1 &= \dot{x}_1 h(x_1, x_2) + g_1(x_1)[f_2(x_1, x_2) + g_2(x_1, x_2)u(t)] \\ &\quad \times h(x_1, x_2) = \frac{df_1}{dt}(x_1) + x_2 \frac{dg_1}{dt}(x_1). \end{aligned} \tag{75}$$

So, we get

$$\begin{aligned} \dot{V} = (&\ddot{x}_{1d} - \dot{x}_1 h(x_1, x_2) - g_1(x_1)[f_2(x_1, x_2) \\ &+ g_2(x_1, x_2)u(t) + \lambda\dot{e}])S. \end{aligned} \tag{76}$$

The control input $u(t)$ should be expressed as given in the following equation, letting $\dot{V}(x) < 0$

$$\begin{aligned} u(t) = &\frac{1}{g_2(x_1, x_2)g_1(x_1)}\Big(\dot{x}_1 h(x_1, x_2) \\ &+ g_1(x_1)f_2(x_1, x_2) - \ddot{x}_{1d} - \lambda\dot{e} - \mu \operatorname{sat}\left(\frac{S}{\varepsilon}\right)\Big) \end{aligned} \tag{77}$$

with

$$\operatorname{sat}\left(\frac{S}{\varepsilon}\right) = \begin{cases} \dfrac{S}{\varepsilon} & \text{if } |e| \leq \varepsilon, \\ \operatorname{sign}\left(\dfrac{S}{\varepsilon}\right) & \text{if } e > \varepsilon, \end{cases} \tag{78}$$

μ and ε are positive design parameters defining the weight of the corrective control part and the boundary layer thickness. □

By substituting Eq. (77) in (76), we get

$$\dot{V} = -\mu \operatorname{sat}\left(\frac{S}{\varepsilon}\right) S \leq 0. \tag{79}$$

Hence, the Lyapunov candidate function (Eq. (73)) decreases gradually which means that $(e, \dot{e})$ converges to 0 as $\to +\infty$. Therefore, the stability in closed-loop is established.

4.1. *Heading control*

The turning motion of the vehicle is given by the following equations:

$$\begin{cases} \dot{\psi} = r, \\ \dot{r} = \dfrac{\tau_{\text{turn}} - g_3(r) + \nabla_1(t)}{I'_z}, \end{cases} \tag{80}$$

where $\nabla_1(t)$ is the compound disturbance in the yaw rate dynamics. It is assumed to be bounded. Hence, there exists a positive constant ∂ such that $\|\nabla_1(t)\| \leq \partial$.

The heading error e_ψ is

$$e_\psi = \psi_d - \psi. \tag{81}$$

The chosen sliding surface S_ψ is

$$S_\psi = \dot{e_\psi} + \lambda e_\psi, \tag{82}$$

λ is a positive design parameter.

Let the candidate Lyapunov function be

$$V_1 = \frac{1}{2} S_\psi^2. \tag{83}$$

Differentiating the Lyapunov function with respect to time gives

$$\begin{aligned} \dot{V}_1 &= S_\psi \dot{S_\psi} \\ &= (\ddot{\psi}_d - \dot{r} + \lambda(\dot{\psi}_d - \dot{\psi}))S_\psi. \end{aligned} \tag{84}$$

By choosing

$$\dot{r} = \ddot{\psi}_d + \lambda(\dot{\psi}_d - \dot{\psi}) + \mu \operatorname{sat}\left(\frac{S_\psi}{\varepsilon}\right), \tag{85}$$

we get

$$\dot{V}_1 = -\mu \operatorname{sat}\left(\frac{S_\psi}{\varepsilon}\right) S_\psi \leq 0 \tag{86}$$

with

$$\operatorname{sat}\left(\frac{S_\psi}{\varepsilon}\right) = \begin{cases} \dfrac{S_\psi}{\varepsilon} & \text{if } |e_\psi| \leq \varepsilon, \\ \operatorname{sign}\left(\dfrac{S_\psi}{\varepsilon}\right) & \text{if } e_\psi > \varepsilon, \end{cases} \tag{87}$$

μ and ε are positive design parameters defining the weight of the corrective control part and the boundary layer thickness.

Using Eqs. (85) and (80), we obtain

$$\begin{aligned} &\ddot{\psi}_d + \lambda(\dot{\psi}_d - r) + \mu \operatorname{sat}\left(\frac{S_\psi}{\varepsilon}\right) \\ &= \frac{\tau_{\text{turn}} - g_3(r) + \nabla_1(t)}{I'_z}. \end{aligned} \tag{88}$$

Therefore

$$\begin{aligned} \tau_{\text{turn}} = g_3(r) - \nabla_1(t) + I'_z\Big((\ddot{\psi}_d + \lambda(\dot{\psi}_d - r) \\ + \mu \operatorname{sat}\left(\frac{S_\psi}{\varepsilon}\right)\Big). \end{aligned} \tag{89}$$

The control input τ_{turn} guarantees the convergence of the trajectory of ψ toward the sliding surface $S_\psi = 0$.

S_ψ will converge to zero, therefore $\dot{e_\psi}$ will converge to $-\lambda e_\psi$. The differential equation $\dot{e_\psi} = -\lambda e_\psi$, therefore, has a solution of the form

$$e_\psi = e^{-\lambda t} e_\psi(t_0). \tag{90}$$

So, the heading error e_ψ will converge exponentially toward 0 and consequently ψ will converge exponentially toward the setpoint ψ_d.

For the determination of constants, $\lambda, \mu, \varepsilon$, we proceed as follows.

During the sliding phase, we have $\dot{e_\psi} = -\lambda e_\psi$. Its characteristic polynomial is

$$P_1(p) = p + \lambda. \tag{91}$$

The sliding time constant is thus $T_1 = \frac{1}{\lambda}$.

During the reaching phase and near the sliding surface (see Fig. 10), we have $|S_\psi| \leq \varepsilon$, so we can pose

$$\lim_{S\psi \to 0} \dot{V}_1 = \lim_{S\psi \to 0} -\mu \operatorname{sat}\left(\frac{S_\psi}{\varepsilon}\right) \cdot S_\psi = -\mu \frac{S_\psi^2}{\varepsilon}, \tag{92}$$

which gives

$$\frac{\dot{V}_1}{V_1} = \frac{-\mu \frac{S_\psi^2}{\varepsilon}}{\frac{1}{2} S_\psi^2} = -2\frac{\mu}{\varepsilon}. \tag{93}$$

The characteristic polynomial is

$$P_2(p) = p + 2\frac{\mu}{\varepsilon}. \tag{94}$$

The sliding time constant is thus

$$T_2 = \frac{\varepsilon}{2\mu}. \tag{95}$$

The reaching phase should be faster than the sliding phase; therefore, the two previous time constants should verify

$$T_2 < T_1.$$

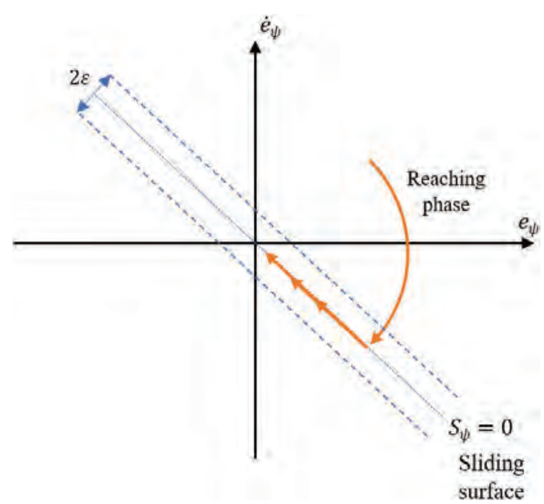

Fig. 10. Phase plan.

For example, we choose $\lambda = 3$, $\mu = 50$ and $\varepsilon = 12$, which gives $T_1 = 0.33\,\mathrm{s}$ and $T_2 = 0.12\,\mathrm{s}$.

4.2. *Speed control*

The differential equation describing the dynamics of the forward speed in the surge is

$$\dot{u} = \frac{\tau_{\text{speed}} + m'rv - g_1(u) + \nabla_2(t)}{m'}, \tag{96}$$

where $\nabla_2(t)$ is the compound disturbance in the surge dynamics. It is assumed to be bounded. Hence, there exists a positive constant ω such that $\|\nabla_2(t)\| \leq \omega$.

The speed error e_u is equal to

$$e_u = u_d - u, \tag{97}$$

where u_d is the desired speed.

The order of Eq. (96) is equal to one, so the sliding surface is $S_u = e_u$.

Let the candidate Lyapunov function be

$$V_2 = \frac{1}{2}e_u^2. \tag{98}$$

Time derivative of Eq. (98) is

$$\dot{V}_2 = e_u\dot{e}_u = (\dot{u}_d - \dot{u})e_u. \tag{99}$$

By choosing

$$\dot{u} = \mu_s \mathrm{sat}\left(\frac{e_u}{\varepsilon_s}\right), \tag{100}$$

μ_s and ε_s are positive design parameters defining the weight of the corrective control part and the boundary layer thickness. μ_s and ε_s were calculated using the same method which was developed in the previous section.

We get

$$\dot{V}_2 = -\mu_s\,\mathrm{sat}\left(\frac{e_u}{\varepsilon_s}\right)\cdot e_u \leq 0, \tag{101}$$

μ_s and ε_s are positive design parameters defining the weight of the corrective control part and the boundary layer thickness.

Using (100) and (96), we obtain

$$\tau_{\text{speed}} = \mu_s\,\mathrm{sat}\left(\frac{e_u}{\varepsilon_s}\right)m' + g_1(u) - m'rv - \nabla_2(t). \tag{102}$$

Thus, the control input τ_{speed} guarantees the convergence of u toward the sliding surface $e_u = 0$.

4.3. *Simulation and results*

In order to analyze the performance of the speed and heading controllers synthesized above, we used MATLAB Simulink with a fixed sample time equal to 10 ms (Fig. 11). The vehicle speed was constrained to follow a desired one $u_d = 1\,\mathrm{m/s}$ and desired headings $\psi_{d1} = 30^\circ$ and $\psi_{d2} = -30^\circ$ as shown in Figs. 13–20. (See the simulation control loop in Fig. 12.)

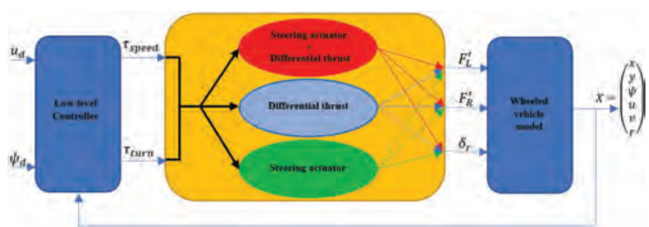

Fig. 11. Low-level controller scheme.

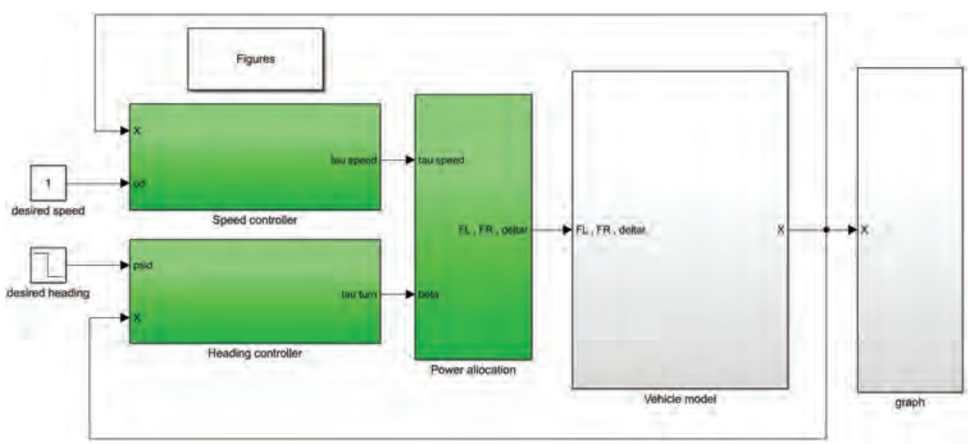

Fig. 12. Simulation control loop.

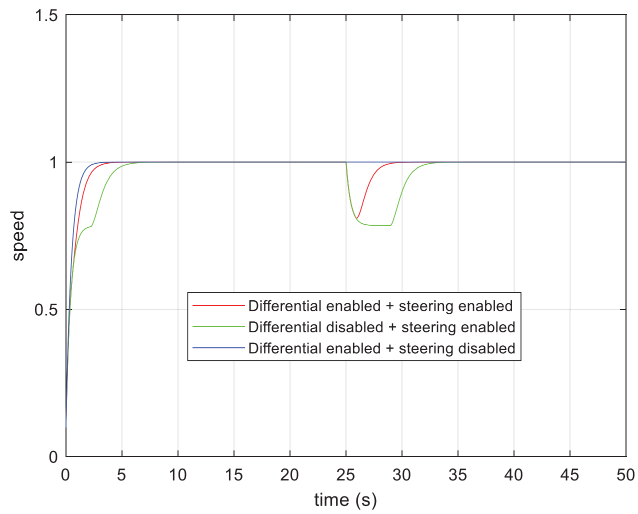

Fig. 13. Time evolution of the surge speed (m/s).

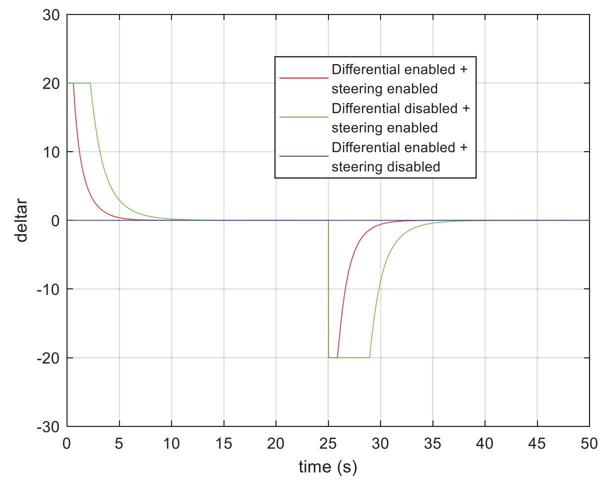

Fig. 15. Input control δ_r ($^\circ$).

Figure 14 shows that the heading angle of the vehicle has converged rapidly and without overshooting toward the desired headings.

Based on the sliding mode control technique, the proposed controller has properly controlled the heading and the speed (Figs. 15–17) of the vehicle as desired. We also note the absence of chattering thanks to the function $\mathrm{sat}(\cdot)$ instead of the function $\mathrm{sign}(\cdot)$ in the τ_{turn} and τ_{speed} expressions.

Figure 18 shows the evolution of the yaw rate. It presents a sudden variation at the beginning; then, it becomes equal to zero when the vehicle reaches its desired heading.

In Fig. 13, we note on the one hand that the surge speed of the vehicle converges without overshooting toward the desired speed and on the other hand that the steady-state error is equal to zero. In the case when the yaw moment

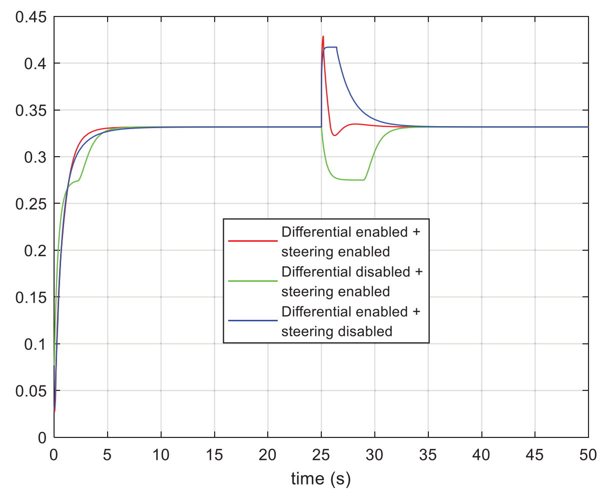

Fig. 16. Input control F_L.

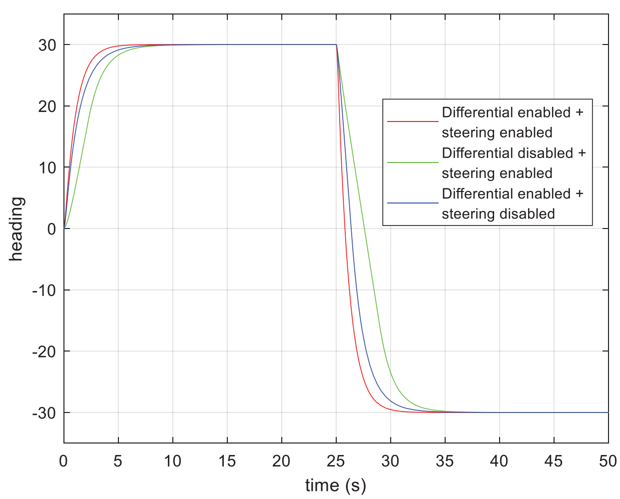

Fig. 14. Heading ($^\circ$).

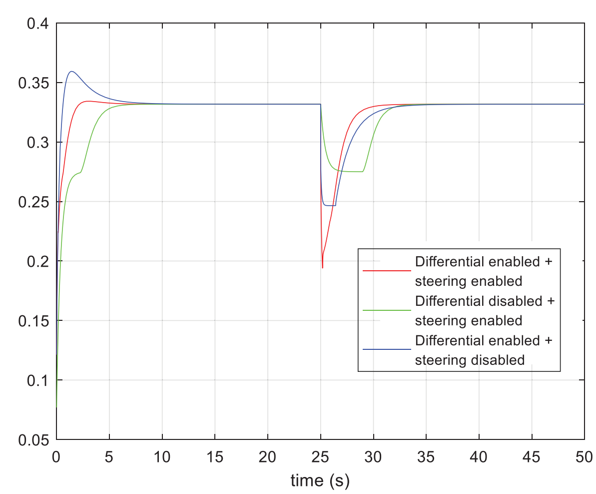

Fig. 17. Input control F_R.

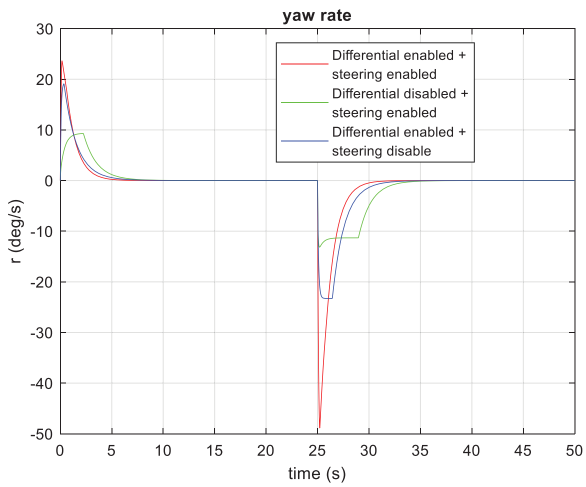

Fig. 18. Time evolution of the yaw rate.

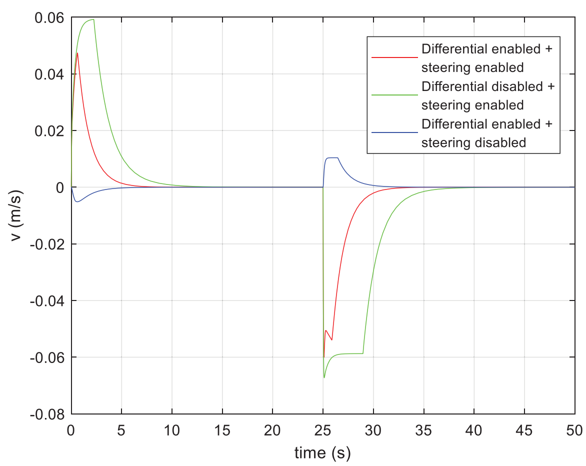

Fig. 19. Time evolution of the sway speed.

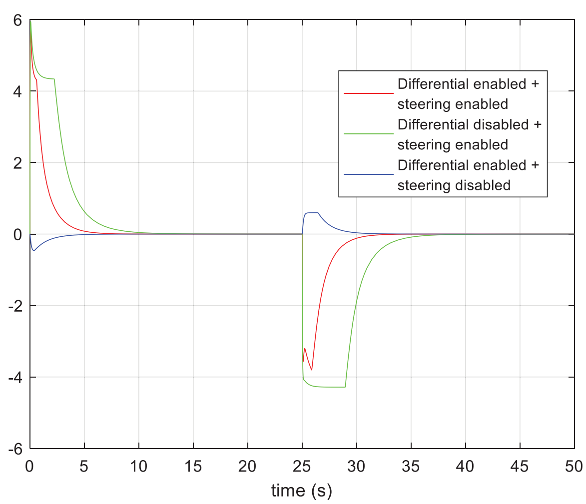

Fig. 20. Time evolution of the side slip angle (°).

controller is designed using only the differential thrust controller, the vehicle speed remains constant and equal to the desired one all the time nevertheless, the vehicle speed shows a slight drop when the yaw moment controller is designed based on the steer actuator.

Figure 20 presents the time evolution of the side slip angle that is caused by the sway speed (Fig. 19) when turning. The side slip angle is small in the case where the yaw moment controller is based only on the differential thrust control.

5. Guidance

In this section, we propose two approaches for generating the desired heading in order to track waypoints and following a given path.

The vehicle self-steering control loop is presented in Fig. 21.

The autopilot (outlined with red color) is mainly composed of two levels of regulation: a low-level regulator for speed and heading control and a high-level controller for waypoints tracking and/or path following control.

5.1. *Heading control*

In the case of waypoint tracking control, the high-level controller allows the vehicle to track a target position (x_d, y_d) by generating the desired heading ψ_d as follows:

$$\psi_d = \text{atan2}(y - y_d, x - x_d), \tag{103}$$

ψ_d represents also the direction of the target position (line of sight — LOS). The LOS algorithm is a widely used method as it is both simple and efficient.

A simulation test was carried out to verify the performance of the developed autopilot as described in Fig. 22.

The parameters used in this simulation are given in Appendix B.

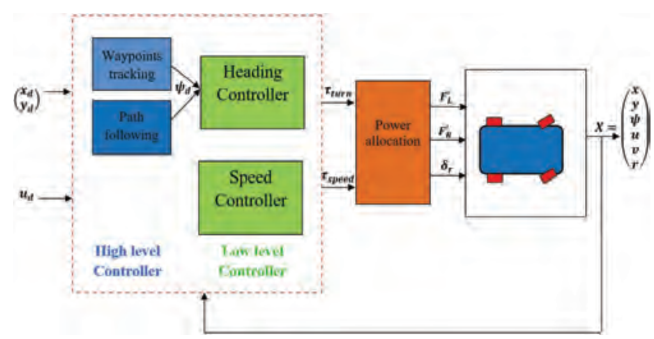

Fig. 21. The vehicle self-driving control loop.

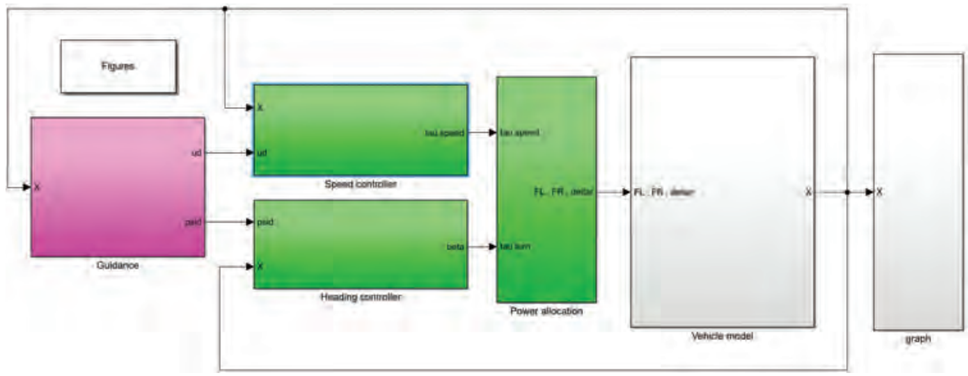

Fig. 22. Simulation control loop.

The initial state vector X_0 is set to $(80\,0\,0\,0\,0\,0\,0)^T$, the desired speed is set to 1 m/s and the desired waypoints are E (90, 20), F (80, 40), G (70, 20), H (80, 0).

Figures 23–31 show the path followed by the vehicle and the time evolution of the system's state during the simulation.

Figure 23 presents the paths followed by the vehicle during the simulation using the three yaw moment control techniques. The greatest trajectory is the one that corresponds to the yaw moment control based on the steer actuator combined with the differential control (red path).

Time evolution of the vehicle heading and speed is illustrated in Figs. 24 and 27. We note that the heading and speed errors are equal to zero in steady-state, highlighting the effectiveness of the sliding mode control techniques used for speed and heading controllers design.

Figure 25 shows the time evolution of the front wheels steering angle during the simulation, it did not exceed, as expected, its maximum value $|\delta_{r_{\max}}| = 20°$. It is equal to 0 in case of the use of only the differential thrust control (blue curve in Fig. 25), in this case, the control input is the difference between the left and the right forces as presented in Figs. 28 and 29. In addition, the side slip angle is small in the case where the yaw moment controller is based only on the differential thrust control as present in Fig. 31 due to the small sway speed in Fig. 30.

Consequently, the LOS guidance successfully fulfilled the principal goals of a guidance system, reaching all desired waypoints.

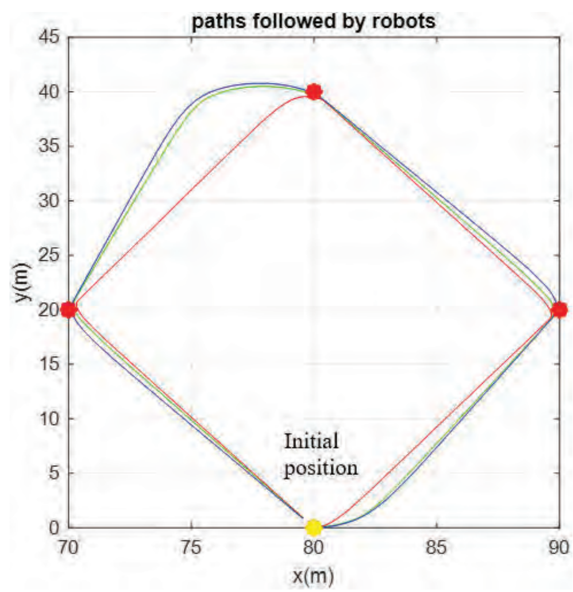

Fig. 23. Path followed by the vehicle during the simulation.

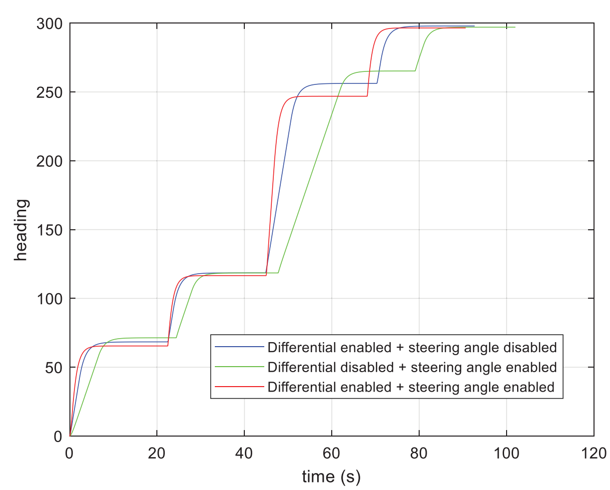

Fig. 24. Heading angle (°).

5.2. *Path following control*

5.2.1. *Second trial: Turning motion*

The line following control is based on the cross-track error; the latter is the shortest distance between the vehicle and the desired path as described in Fig. 33. Consequently, it is desirable to minimize this error in order to follow the path

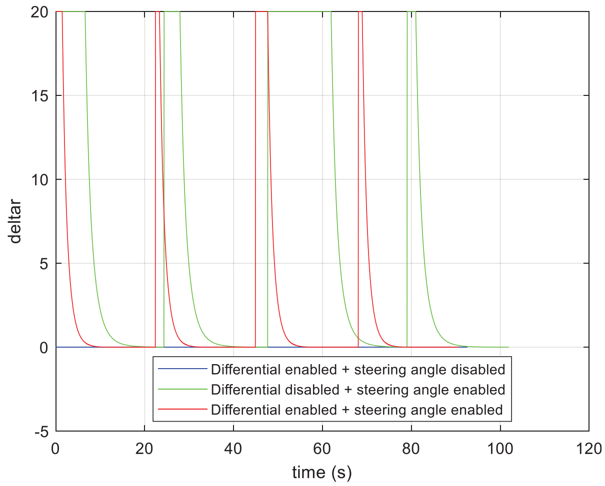

Fig. 25. Input control δ_r (°).

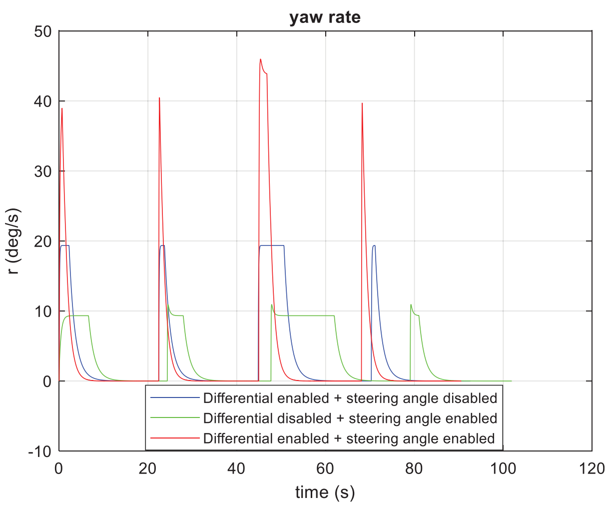

Fig. 26. Yaw rate.

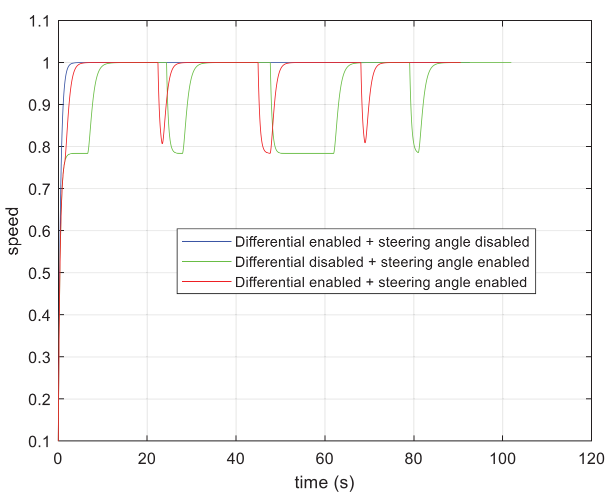

Fig. 27. Surge speed (m/s).

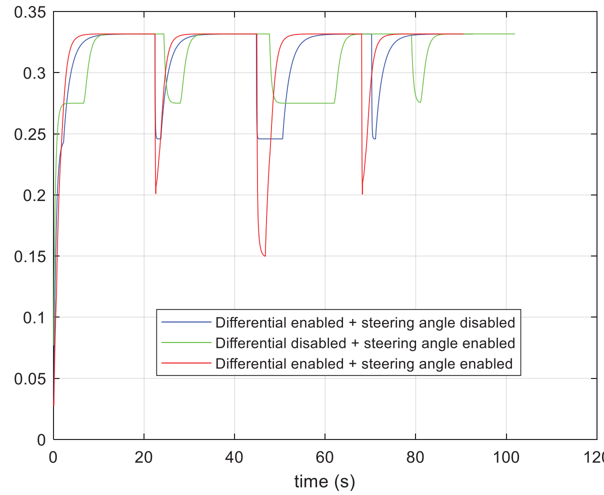

Fig. 28. Left thrust force.

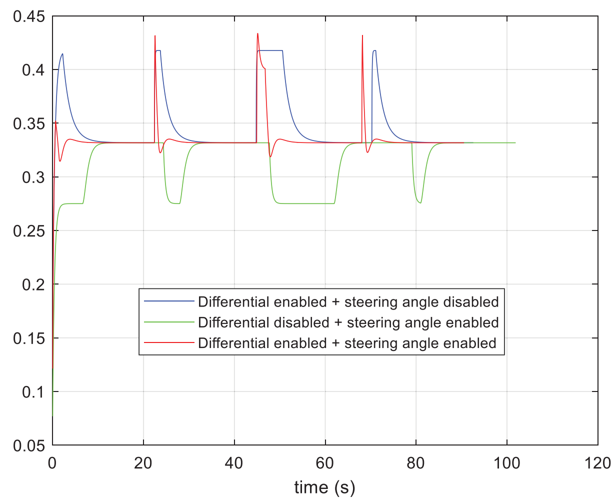

Fig. 29. Right thrust force.

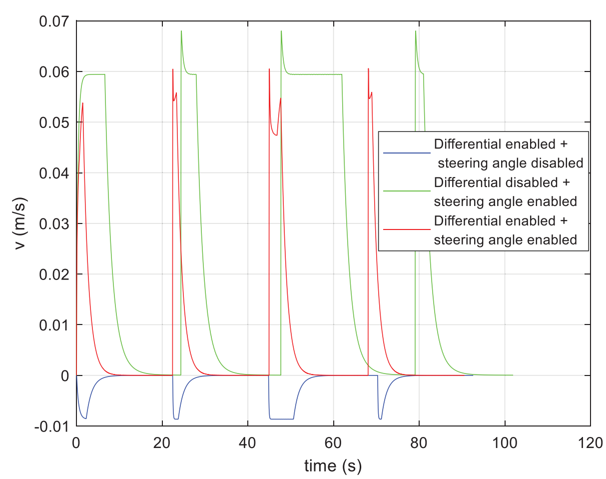

Fig. 30. Sway speed.

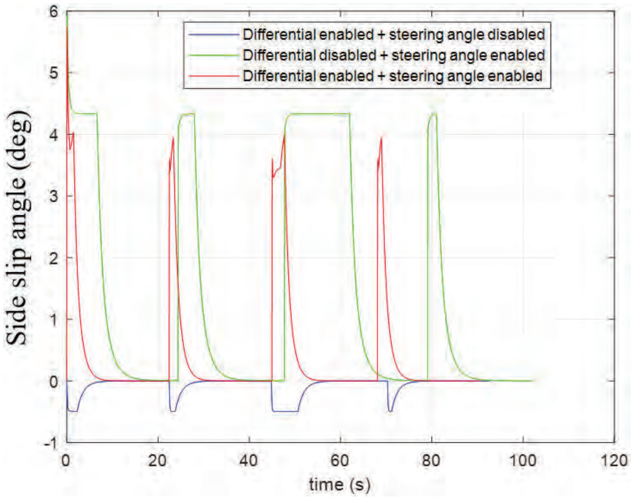

Fig. 31. Side slip angle (°).

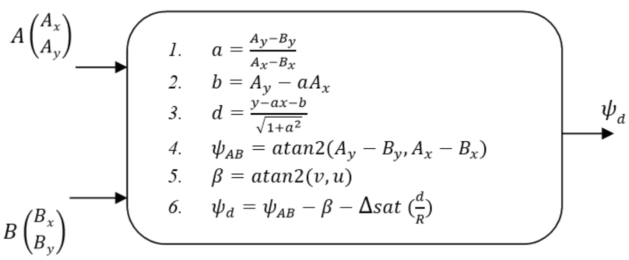

Fig. 32. Algorithm for line following controller.

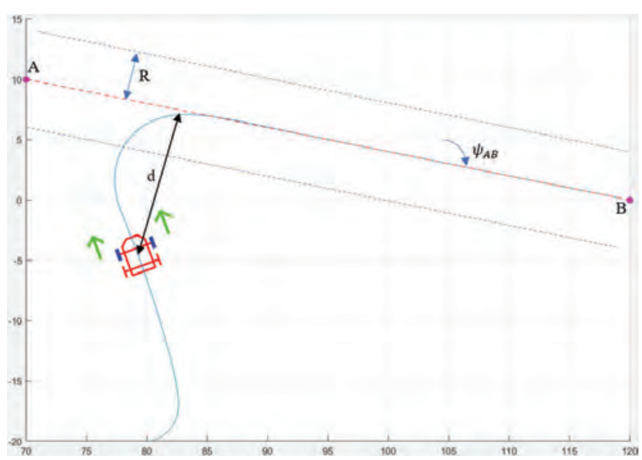

Fig. 33. Line following explication.

as tightly as possible. Therefore, it is recommended to design a desired heading ψ_d depending on this error letting the vehicle to converge to a desired path and to remain on it precisely. In this context, we propose the following control algorithm (Fig. 32).

where a, b, d, ψ_{AB} and β are defined below and R represents the width of the safety lane.

The algebraic distance d between the vehicle current position (x, y) and the (AB) trajectory to follow is calculated using the following equation:

$$d = \frac{y - ax - b}{\sqrt{1 + a^2}} \tag{104}$$

with

- $a = \frac{y_A - y_B}{x_A - x_B}$: slope of the line (AB) in the fixed coordinate system,
- $b = y_A - a x_A$,
- $\beta = a\tan 2(v, u)$,
- ψ_{AB} : The angle between the line (AB) and X-axis of the fixed coordinate system. It is calculated using the following expression:

$$\psi_{AB} = a\tan 2(y_A - y_B, x_A - x_B). \tag{105}$$

We check that

$$\tan \psi_{AB} = a. \tag{106}$$

The desired heading angle is given by

$$\psi_d = \psi_{AB} - \beta - \Delta \operatorname{sat}\left(\frac{d}{R}\right), \tag{107}$$

where $\Delta > 0$ is an adjustment parameter that determines the angle of incidence on the desired trajectory ($\Delta = \pi/2$ when the vehicle is far from the safety corridor).

The time derivative of the algebraic distance d is calculated as follows:

$$\begin{aligned}\dot{d} &= \frac{1}{\sqrt{1+a^2}}(\dot{y} - a\dot{x}) \\ &= \frac{1}{\sqrt{1+a^2}}(u \sin\psi + v\cos\psi - au\cos\psi + av\sin\psi) \\ &= \frac{1}{\sqrt{1+a^2}}(u(\sin\psi - a\cos\psi) + v(\cos\psi + a\sin\psi)).\end{aligned} \tag{108}$$

Using the following trigonometric relationships

$$\tan^{-1} x + \tan^{-1}\frac{1}{x} = \frac{\pi}{2}, \tag{109}$$

$$c_1 \cos x + c_2 \sin x = \sqrt{c_1^2 + c_2^2}\cos\left(x - \tan^{-1}\frac{c_2}{c_1}\right), \tag{110}$$

Eq. (33) becomes

$$\begin{aligned}\dot{d} = \frac{1}{\sqrt{1+a^2}}\Bigg(& u\sqrt{1+a^2}\cos\left(\psi - \tan^{-1}\frac{1}{-a}\right) \\ &+ v\sqrt{1+a^2}\cos(\psi - \tan^{-1} a)\Bigg)\end{aligned}$$

$$= \frac{1}{\sqrt{1+a^2}}\left(u\sqrt{1+a^2}\cos\left(\psi - \left(\frac{\pi}{2} - \tan^{-1}(-a)\right)\right.\right.$$
$$\left.+ v\sqrt{1+a^2}\cos(\psi - \tan^{-1}a)\right)$$
$$= \frac{1}{\sqrt{1+a^2}}(u\sqrt{1+a^2}\sin(\psi - \psi_{AB})$$
$$+ v\sqrt{1+a^2}\cos(\psi - \psi_{AB}))$$
$$= u\sin(\psi - \psi_{AB}) + v\cos(\psi - \psi_{AB}). \tag{111}$$

We obtain

$$\dot{d} = \sqrt{u^2+v^2}\sin(\psi - \psi_{AB} + \beta). \tag{112}$$

Using (112) and assuming the desired heading is perfectly followed $\psi = \psi_d$ so that the system converges to the surface $d = 0$. If we assume that the desired heading is perfectly followed and we choose the desired heading angle ψ_d as given with Eq. (107), the derivative of the algebraic distance d becomes

$$\dot{d} = -\sqrt{u^2+v^2}\sin\left(\Delta\,\mathrm{sat}\left(\frac{d}{R}\right)\right). \tag{113}$$

Consider the following Lyapunov candidate function:

$$V_L = \frac{1}{2}d^2. \tag{114}$$

Its derivative with respect to time is

$$\dot{V}_L = \dot{d}d$$
$$= -\sqrt{u^2+v^2}\sin\left(\Delta\,\mathrm{sat}\left(\frac{d}{R}\right)\right)d. \tag{115}$$

By choosing $\Delta < \pi$, we get $\dot{V}_L < 0$. In this case, we can consider that V_L is a Lyapunov function for the trajectory $d = 0$.

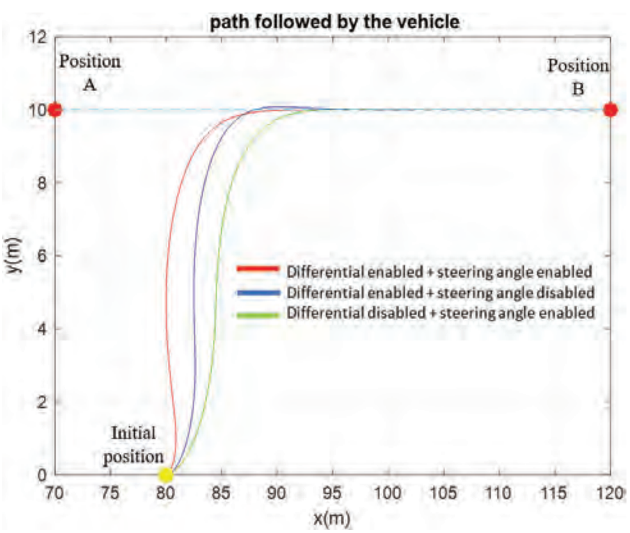

Fig. 34. Path followed by the vehicle.

Consequently, the control law (Eq. (107)) defining the desired heading angle guarantees the convergence of the distance d toward zero as shown in Figs. 35–42.

5.2.2. *Obstacle avoidance control*

In this section, we propose the analysis of the behavior of the vehicle when an obstacle is encountered during way-point tracking and path following control.

To avoid collision with an obstacle, we propose the following algorithm:

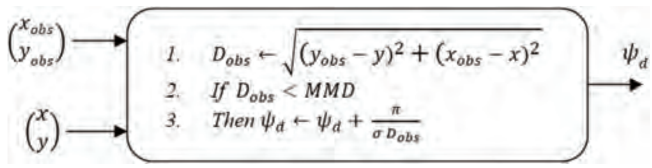

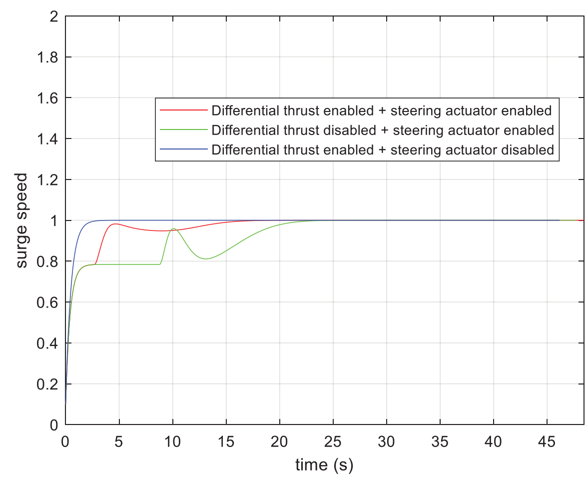

Fig. 35. Surge speed (m/s).

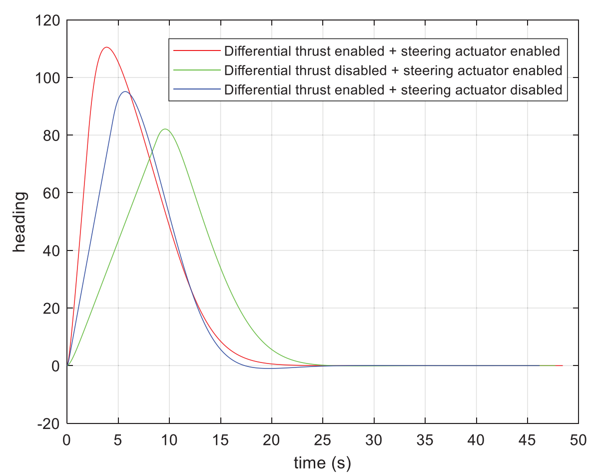

Fig. 36. Heading angle (°).

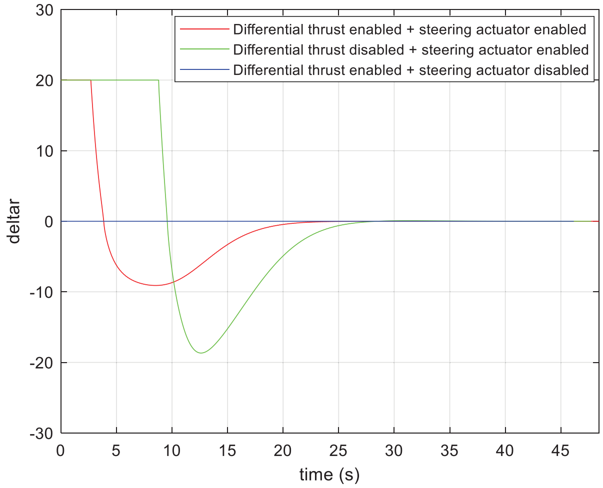

Fig. 37. Steering angle (°).

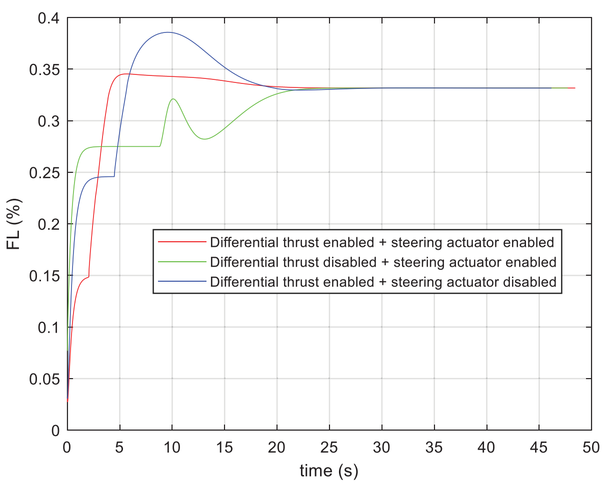

Fig. 38. Left thrust.

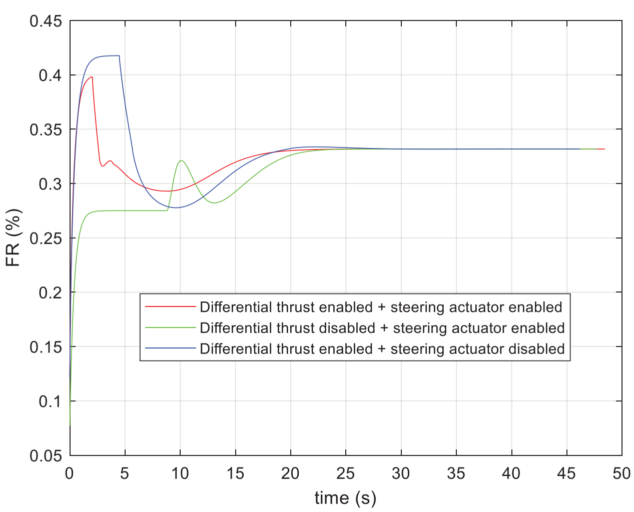

Fig. 39. Right thrust.

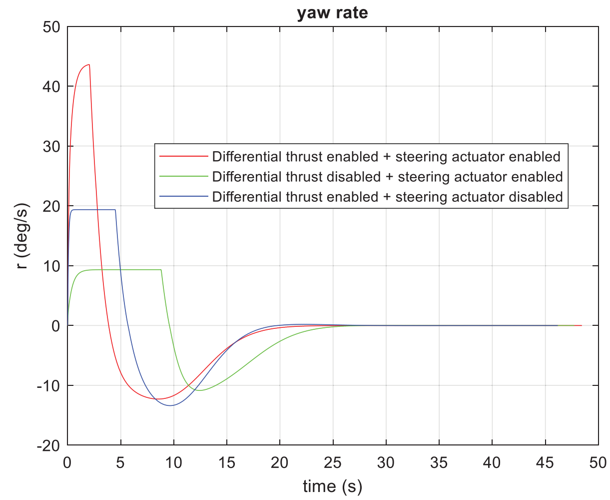

Fig. 40. Yaw rate.

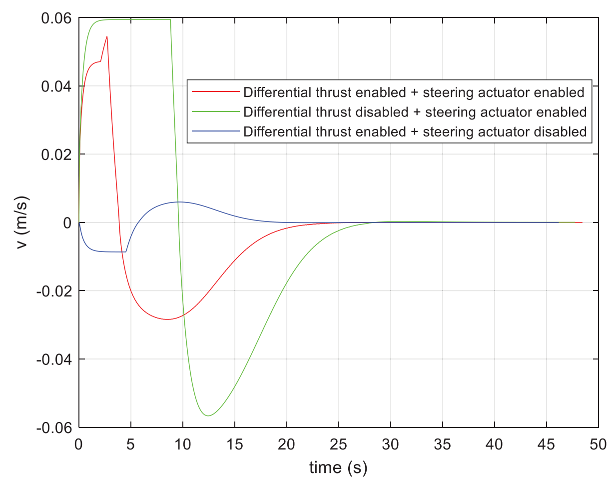

Fig. 41. Sway speed.

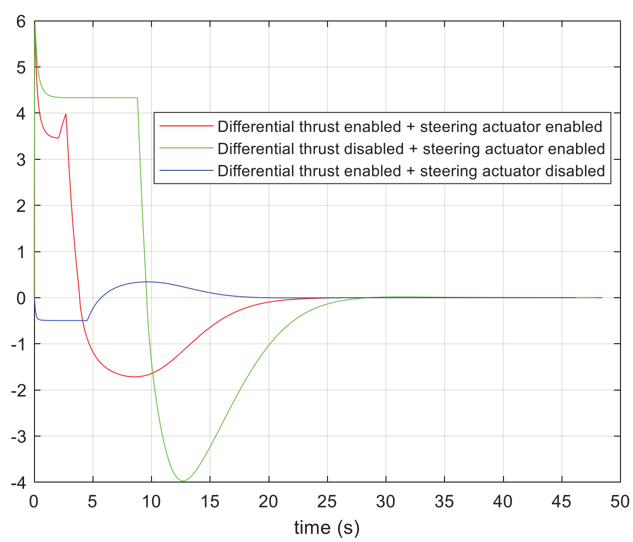

Fig. 42. Side slip angle (°).

This approach consists of updating the desired heading ψ_d, which is generated by the high-level controller, in order to avoid an encountered obstacle at position (x_{obs}, y_{obs}).

Where MMD is the minimum maneuvering distance, it was chosen depending on the vehicle speed. D_{obs} is the distance between the vehicle and the obstacle. σ is a design control parameter.

Figures 43 and 44 present the paths followed by the vehicle, we can conclude that the three techniques for yaw moment controller design have the same responses in terms of safety and maneuver rapidity when the vehicle has to avoid collision with an encountered obstacle.

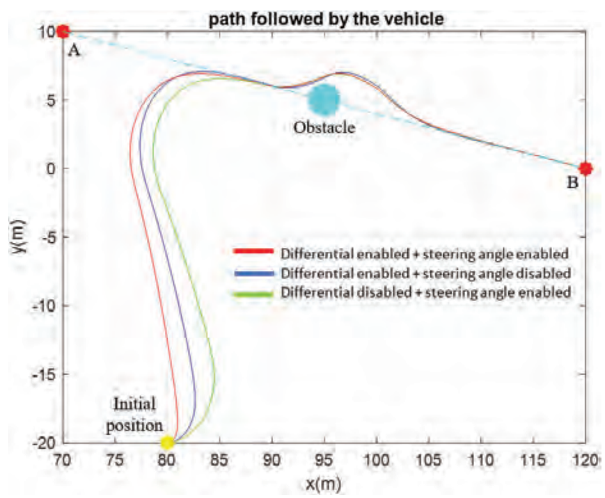

Fig. 43. Obstacle avoidance when following a desired path.

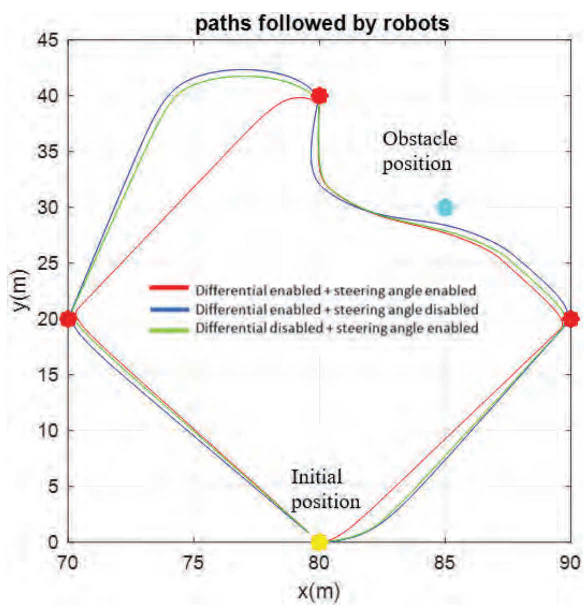

Fig. 44. Obstacle avoidance when tracking waypoints.

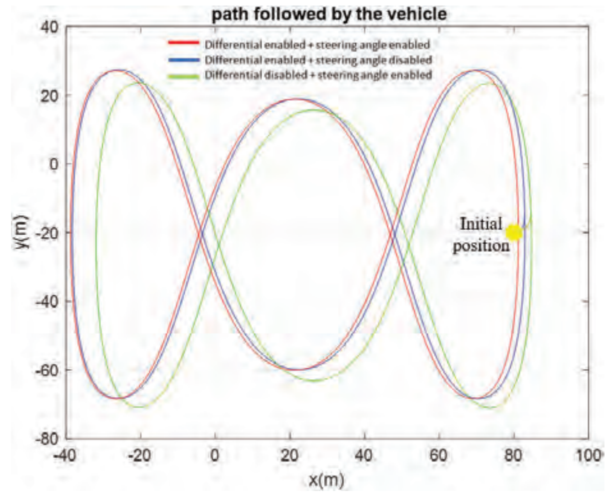

Fig. 45. Path followed by the vehicle.

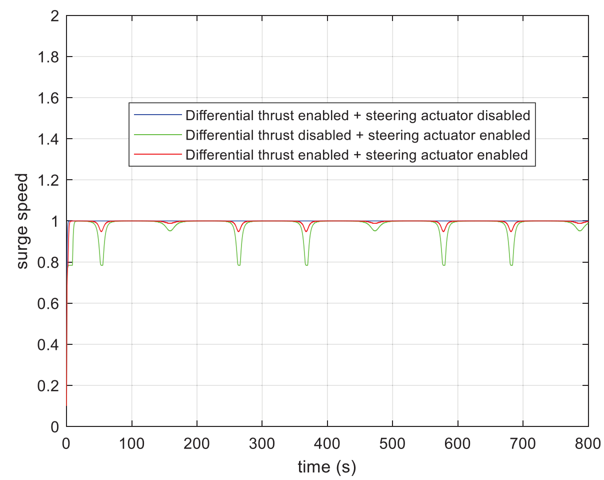

Fig. 46. Vehicle speed (m/s).

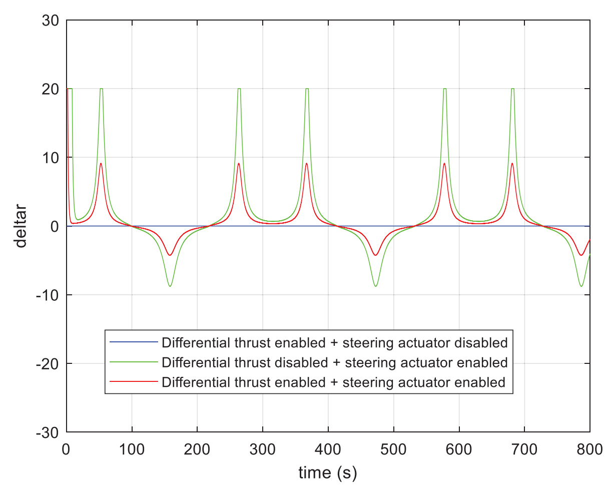

Fig. 47. Steering angle (°).

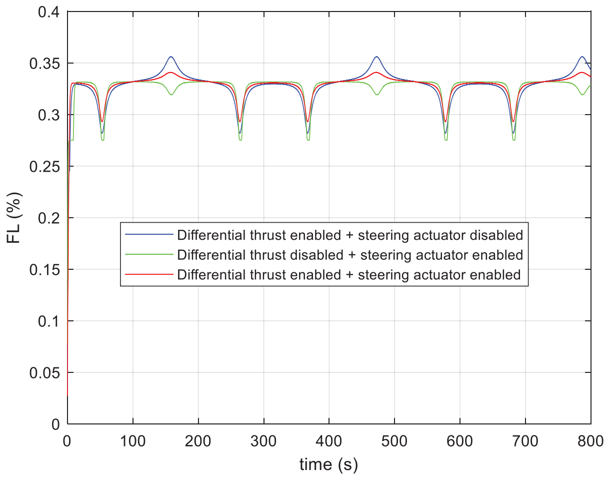

Fig. 48. Left thrust.

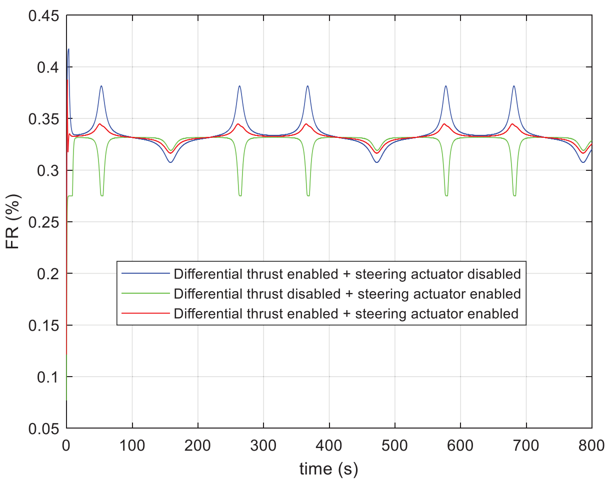

Fig. 49. Right thrust.

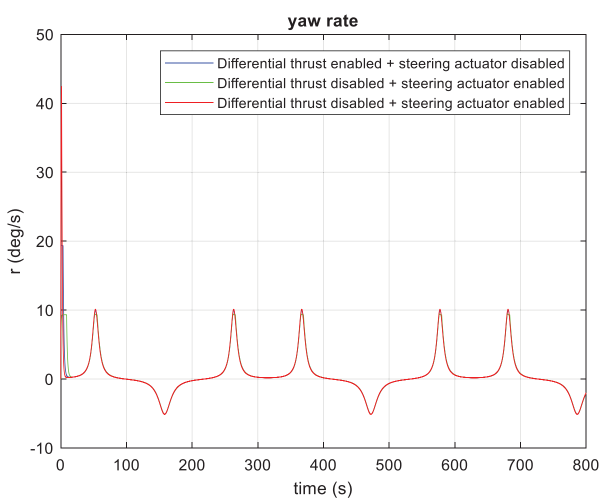

Fig. 50. Yaw rate.

5.2.3. *Lissajous curve control*

In order to further test the effectiveness of the designed autopilot, we enforced the vehicle to follow a complex temporal assigned path (Lissajous path). The high-level controller generates in this case the following desired heading:

$$\psi_d = \text{atan2}(\dot{y}_d, \dot{x}_d) \tag{116}$$

with

$$x_d = 10\cos(0.01t), \tag{117}$$

$$y_d = 10\sin(0.03t). \tag{118}$$

The vehicle's tracking of the Lissajous path is shown in Fig. 45. It is obvious that the reference path is well followed

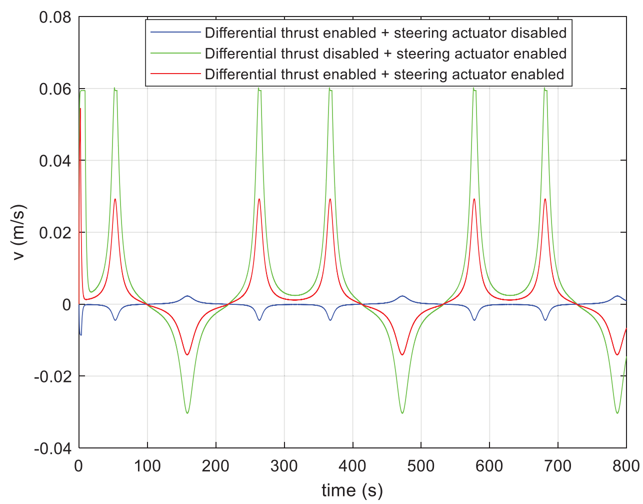

Fig. 51. Sway velocity.

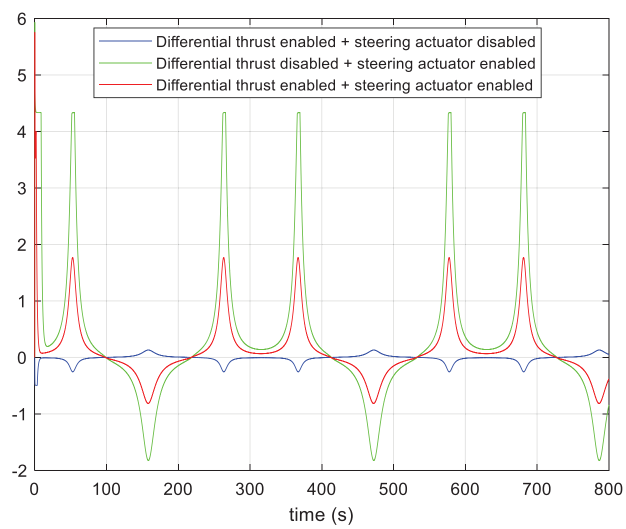

Fig. 52. Side slip angle ($^\circ$).

by the vehicle in spite of its complexity. Time evolution of the system states is presented in Figs. 46–52.

6. Experimental Results

After testing the performances of the designed controllers by simulation in the previous section, we can conclude that the yaw moment controller based on the differential thrust control and steering angle control is the best technique for the vehicle waypoint tracking control. In this context, a microcontroller-based autopilot system is designed in this section allowing the vehicle to control its heading in order to track desired positions and to avoid any encountered obstacle.

The material architecture of the designed autopilot is presented in Figs. 53 and 54. It consists of an inertial measurement unit (IMU) (MPU9250) for the measurements of the vehicle heading and yaw rate; it is mounted far from the main electric circuit in order to minimize the magnetic effects. A GPS receiver for measuring the current position of the vehicle. An SD card reader is also used for data logging (GPS positions, heading angle, output control signal, etc.). A Jetson nanomicrocomputer is employed, interfacing with both the microcontroller and the RPLIDAR via USB, to manage the obstacle avoidance process. The Jetson nano processes the laser scan data, calculates a correction to the desired heading (algorithm presented in Sec. 5.2.2) and applies it to steer the vehicle. This computation is performed through a Python script utilizing the ROS client library (rclpy), ensuring real-time responsiveness and precise navigation. The designed yaw moment controller based on the sliding mode technique ($\lambda = 3$, $\mu = 50$, $\varepsilon = 12$) is implemented using an ATmega2560 microcontroller with a sampling time T_s equal to 0.01 s. In this section, the thrust force τ_{speed} is kept constant and equal to 35% to provide a speed equal to 1 m/s.

Fig. 53. Vehicle description.

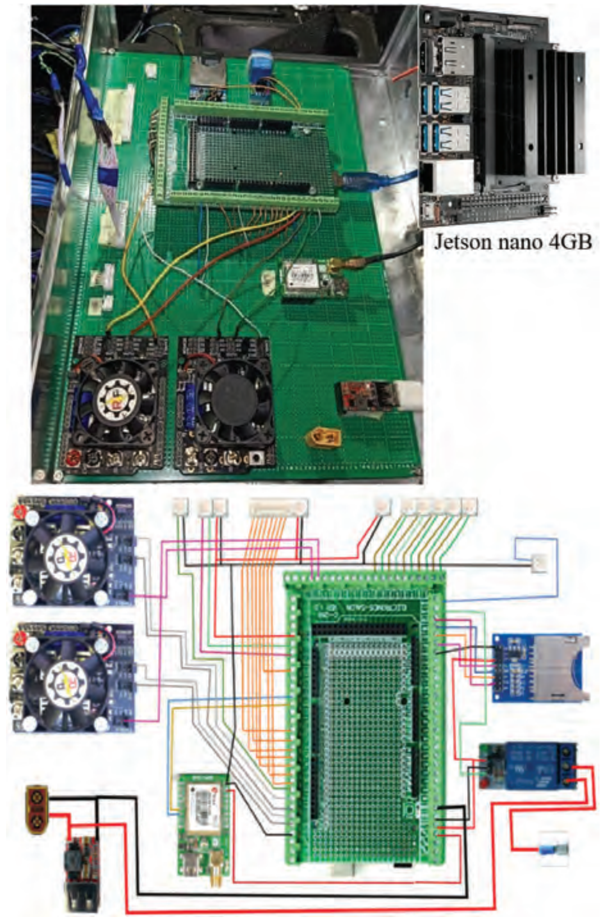

Fig. 54. Hardware architecture of the autopilot system.

First, an indoor experimental test was carried out to show the behavior of the vehicle when tracking a desired heading angle equal to 30° then to 45°.

The blue curve in the following figure represents the real-time evolution of the vehicle heading (recorded on the SD memory card).

The experimental results (Fig. 55) show that the vehicle heading converges to the desired ones with some fluctuations (Fig. 56).

Figure 57 shows the steering angle of the front wheel when tracking desired headings.

A second experimental test was carried out to demonstrate the effectiveness of the autopilot system for waypoint tracking control (see Appendix A). Figure 58 shows the path followed by the vehicle during the second trial. The vehicle rallied all the desired positions as expected and avoided an encountered obstacle using an RPLIDAR 360 integrated with the embedded system to detect and maneuver around the obstacle.

From Figs. 61 and 62, it is noted that the produced control input for the steering angle presents fluctuations all

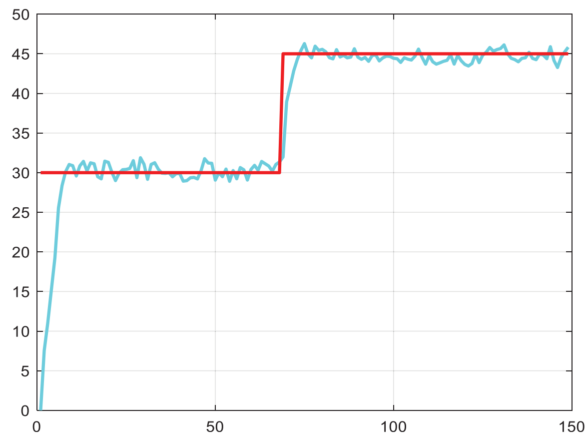

Fig. 55. Heading (°) tracking during experimental results ($T_s = 00.1$ s).

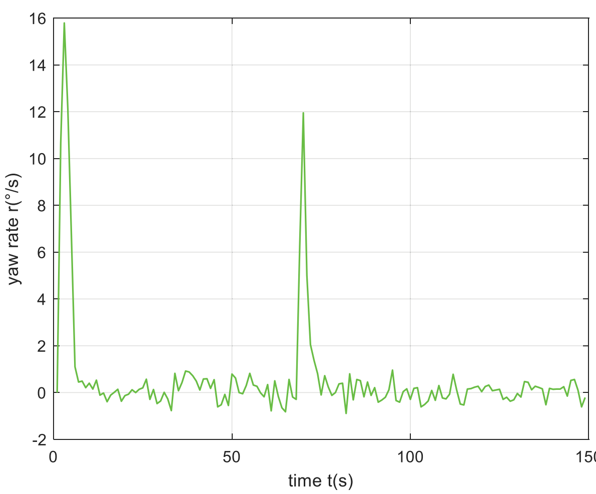

Fig. 56. Yaw rate during experimental result ($T_s = 001$ s).

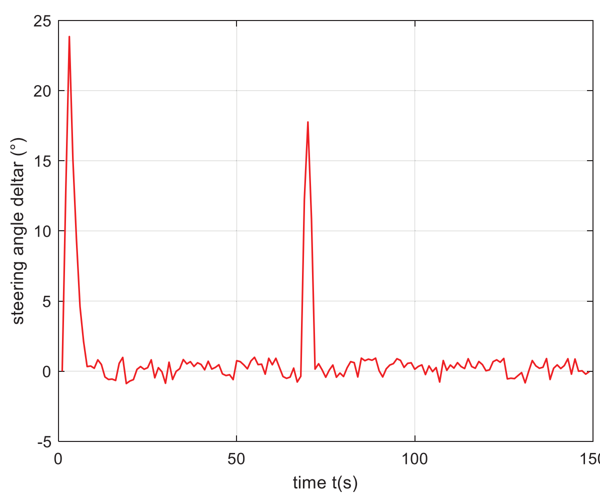

Fig. 57. Steering angle during simulation and experimental results ($T_s = 001$ s).

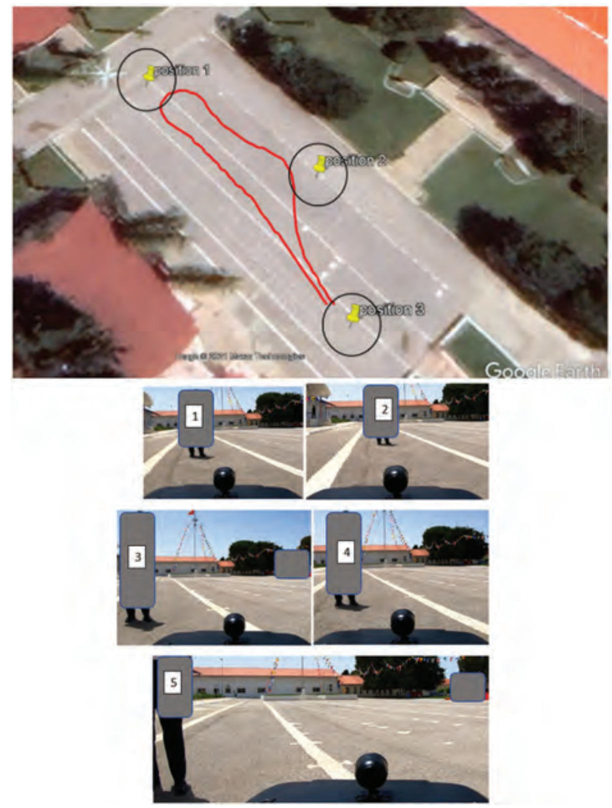

Fig. 58. Path followed by the vehicle during the experimental test while avoiding an encountered obstacle.

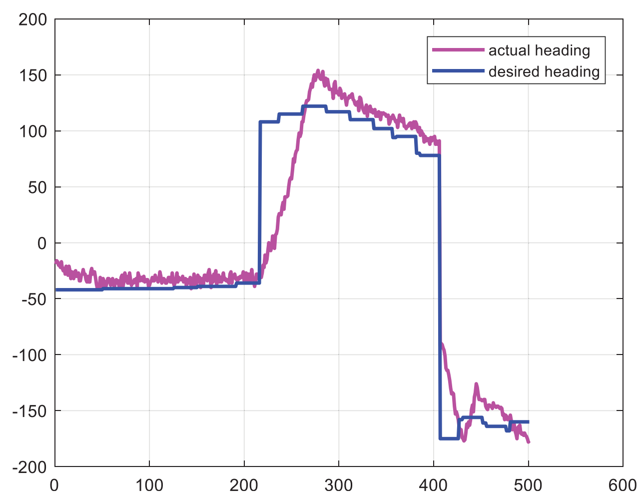

Fig. 59. Time evolution of the heading angle (°).

the time due to the heading measurement noise from the IMU sensor as described in Fig. 59. It is also noted that the vehicle orientation converges rapidly and without overshooting to the desired heading as present in Figs. 59 and 60.

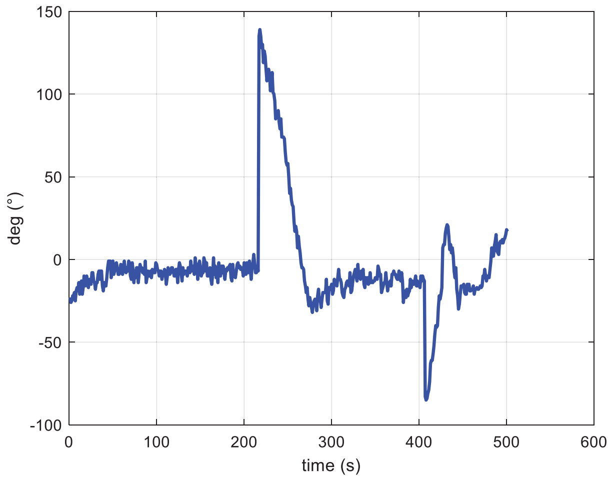

Fig. 60. Time evolution of the heading error between the actual value and the desired one during the experimental test ($T_s = 001\,\mathrm{s}$).

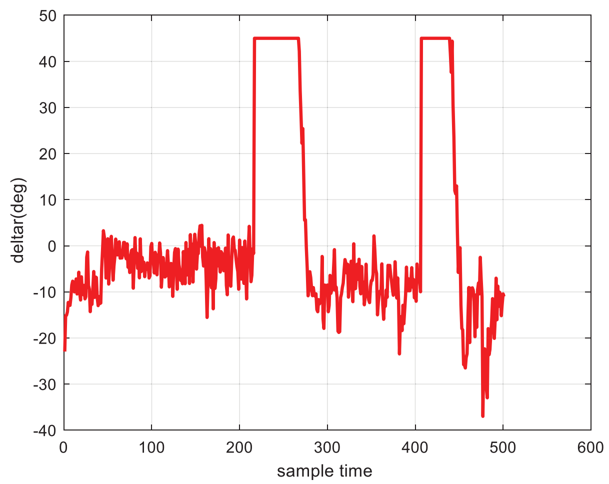

Fig. 61. Evolution of the steering servo angle (actuator for controlling the steering angle δr).

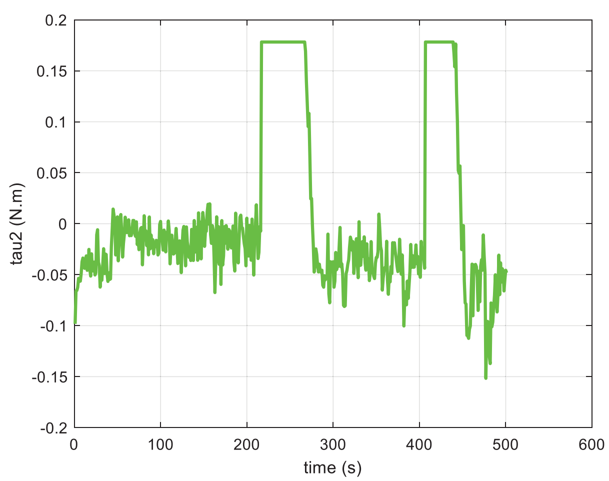

Fig. 62. Evolution of the yaw moment.

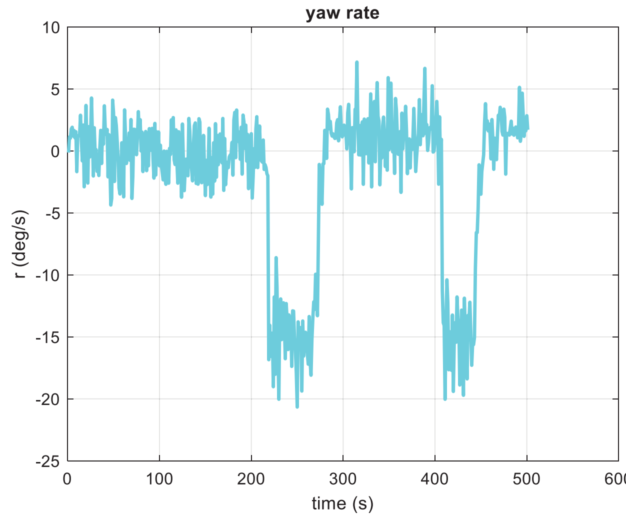

Fig. 63. Time evolution of the yaw rate ($T_s = 001\,\mathrm{s}$).

These good tracking performances clearly show the efficiency of the proposed control approach.

Figure 63 shows the time evolution of the yaw rate, we can conclude that the maximum yaw rate does not exceed the value of 20°/s as demonstrated in the identification section.

Consequently, the obtained results show that the designed autopilot system based on the yaw moment controller is efficient in achieving a waypoint tracking control.

7. Conclusion

This paper proposes the design of a guidance, navigation and control (GNC) system for an unmanned wheeled vehicle.

The vehicle mathematical modeling with 3DOF was developed first to create a simulation environment and its parameters are afterward identified experimentally.

Based on the Lyapunov theory, two control laws were synthesized to control the heading and the speed of the vehicle, after that, a theoretical approach has been established to tune the control parameters. A guidance system was also designed letting the vehicle track a target position and follow a desired path in the presence of an obstacle. A power allocation system was also designed in order to be able to control the vehicle heading using three techniques for yaw moment control; only differential thrust control, only steering angle control and both together. The global yaw moment control (differential thrust and steer control are both enabled) was the best technique for waypoint tracking control and path following control. Nonetheless, yaw moment controller using only the differential thrust technique was the best one for controlling the speed of the vehicle. In addition, the three techniques show good behavior for obstacle avoidance.

Finally, an autopilot system was developed, in real-time, using the yaw moment control technique based on the steering actuator control combined with the differential thrust control and some trials were done to show the behavior of the vehicle when tracking desired waypoints.

Moreover, the results obtained open up broad prospects, such as the design of an autopilot allowing the vehicle to follow a given path instead of waypoint tracking control.

Acknowledgment

The authors would like to thank the Ministry of Defense, the Naval Academy of Tunisia and the Tunisian Ministry of Higher Education and Scientific Research for supporting this work.

Appendix A

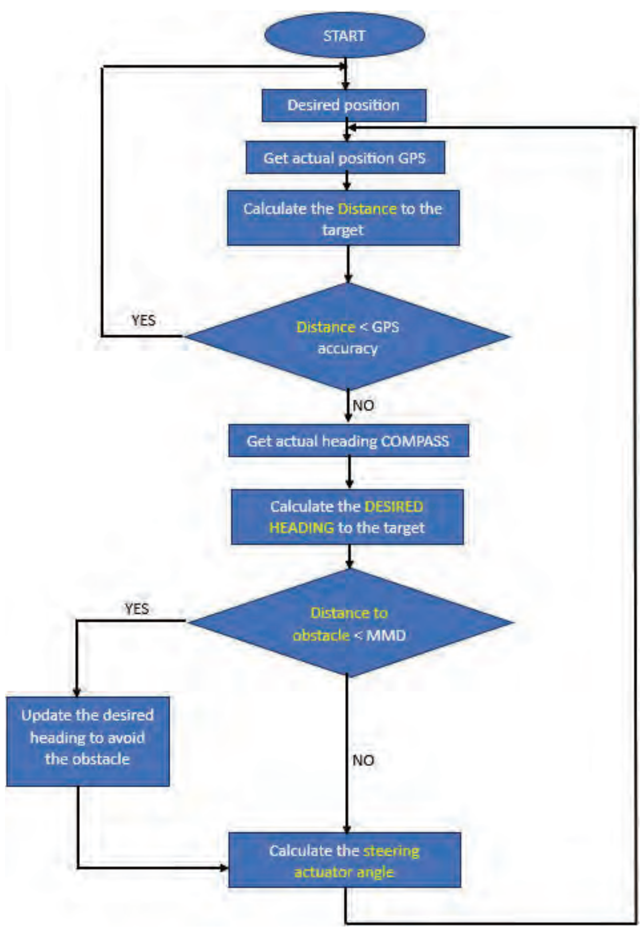

Appendix B

Coefficient	Value
I_Z	$5.841\ \mathrm{kg \cdot m^2}$
I'_Z	0.0128
m	37 kg
m'	0.0768
α_1	1.3268
β_1	0.8933
α_2	0.3028
β_2	0.8250
α_3	3
d	0.36 m
g	$9.8\ \mathrm{ms^{-2}}$
T	0.02 s
T_s	0.01 s

ORCID

Helmi Abrougui https://orcid.org/0000-0001-6005-2046
Samir Nejim https://orcid.org/0000-0001-7777-5427

References

[1] Y. Kim and B. K. Kim, Efficient time-optimal two-corner trajectory planning algorithm for differential-driven wheeled mobile robots with bounded motor control inputs, *Rob. Auton. Syst.* **64** (2015) 35–43.

[2] I. Kanellakopoulos and P. V. Kokotovic, Systematic design of adaptive controllers for feedback linearizable systems, *IEEE Trans. Autom. Control* **36**(11) (1991) 1241–1253.

[3] Y. Feng, X. Yu and Z. Man, Non-singular terminal sliding mode control of rigid manipulators, *Automatica* **38**(12) (2002) 2159–2167.

[4] S. P. Bhat and D. S. Bernstein, Finite-time stability of homogeneous systems, in *Proc. American Control Conf.*, Vol. 4 (IEEE, 1997), pp. 2513–2514.

[5] W. Q. Tang and Y. L. Cai, High-order sliding mode control design based on adaptive terminal sliding mode, *Int. J. Robust Nonlinear Control* **23**(2) (2013) 149–166.

[6] C. Y. Chen, T. H. S. Li, Y. C. Yeh and C. C. Chang, Design and implementation of an adaptive sliding mode dynamic controller for wheeled mobile robots, *Mechatronics* **19**(2) (2009) 156–166.

[7] M. Ou, H. Du and S. Li, Finite-time tracking control of multiple nonholonomic mobile robots, *J. Franklin Inst.* **349**(9) (2012) 2834–2860.

[8] J. Yang, Q. Wang and Y. Li, An improved second order sliding mode twisting algorithm for finite-time trajectory tracking of intelligent vehicle, *Adv. Mech. Eng.* **5** (2013) 1–8.

[9] A. S. Al-Araji, M. F. Abbod and H. S. Al-Raweshidy, Applying posture identifier in designing an adaptive nonlinear predictive controller for nonholonomic mobile robot, *Neurocomputing* **99** (2013) 543–554.

[10] D. Chwa, Fuzzy adaptive tracking control of wheeled mobile robots with state-dependent kinematic and dynamic disturbances, *IEEE Trans. Fuzzy Syst.* **20**(3) (2012) 587–593.

[11] F. Yang and C. Wang, Adaptive tracking control for uncertain dynamic nonholonomic mobile robots based on visual servoing, *J. Control Theory Appl.* **10**(1) (2012) 56–63.

[12] S. Blažič, A novel trajectory-tracking control law for wheeled mobile robots, *Rob. Auton. Syst.* **59** (2011) 1001–1007.
[13] Z. Man and O. Mike, A robust adaptive terminal sliding mode control for rigid robotic manipulators, *J. Intell. Rob. Syst.* **24**(1) (1999) 23–41.
[14] D. Z. Feng, Z. Bao and L. C. Jiao, Total least mean squares algorithm, *IEEE Trans. Signal Process.* **46**(8) (1998) 2122–2130.
[15] R. Martinek, J. Rzidky, R. Jaros, P. Bilik and M. Ladrova, Least mean squares and recursive least squares algorithms for total harmonic distortion reduction using shunt active power filter control, *Energies* **12**(8) (2019) 1545.
[16] U. Kiencke and L. Nielsen, *Automotive Control Systems: For Engine, Driveline, and Vehicle* (Springer, 2000).
[17] X. Xiong, Artificial intelligence control algorithm for the steering motion of wheeled soccer robot, *Int. J. Pattern Recognit. Artif. Intell.* **33**(10) (2019) 1959034.
[18] P. Murrieri, D. Fontanelli and A. Bicchi, A hybrid-control approach to the parking problem of a wheeled vehicle using limited view-angle visual feedback, *Int. J. Rob. Res.* **23**(4–5) (2004) 437–448.
[19] H. F. Grip, L. Imsland, T. A. Johansen, J. C. Kalkkuhl and A. Suissa, Vehicle sideslip estimation — Design, implementation and experimental validation, *IEEE Control Syst. Mag.* **29**(5) (2009) 36–52.
[20] A. Boyali, S. Mita and V. John, A tutorial on autonomous vehicle steering controller design, simulation and implementation, preprint (2018), arXiv:1803.03758.
[21] X. Diao *et al.*, Composite active front steering controller design for vehicle system, *IEEE Access* **5** (2017) 6697–6706.
[22] M. Park, S. Lee and W. Han, Development of steering control system for autonomous vehicle using geometry-based path tracking algorithm, *ETRI J.* **37**(3) (2015) 617–625.
[23] Q. Xu *et al.*, Wheel deflection control of agricultural vehicles with four-wheel independent omnidirectional steering, *Actuators* **10**(12) (2021) 334.
[24] D. Yin, J. Wang, J. Du, G. Chen and J. Hu, A new torque distribution control for four-wheel independent-drive electric vehicles, *Actuators* **10**(6) (2021) 122.
[25] L. Chen, P. Li, W. Lin and Q. Zhou, Observer-based fuzzy control for four-wheel independently driven electric vehicles with active steering systems, *Int. J. Fuzzy Syst.* **22** (2020) 89–100.
[26] H. Sun, H. Li, Y. Li, Z. Song and K. Xu, Accelerating the validation of motion control for a 4WD4WS ground vehicle using a hierarchical controller hardware-in-the-loop system, in *Proc. 2019 IEEE Int. Conf. Robotics and Biomimetics (ROBIO)* (IEEE, 2019), pp. 2396–2401.
[27] Z. Yutian, N. Jun, T. Hanqing, W. Wei and H. Jibin, Integrated robust dynamics control of all-wheel-independently-actuated unmanned ground vehicle in diagonal steering, *Mech. Syst. Signal Process.* **164** (2022) 108263.
[28] B. Ren, H. Chen, H. Zhao and L. Yuan, MPC-based yaw stability control in in-wheel-motored EV via active front steering and motor torque distribution, *Mechatronics* **38** (2016) 103–114.
[29] M. A. Khan *et al.*, Robust differential steering control system for an independent four wheel drive electric vehicle, *Int. J. Automot. Technol.* **20** (2019) 87–97.
[30] J. Tian, J. Tong and S. Luo, Differential steering control of four-wheel independent-drive electric vehicles, *Energies* **11**(11) (2018) 2892.
[31] G. Klančar, D. Matko and S. Blažič, A control strategy for platoons of differential drive wheeled mobile robot, *Rob. Auton. Syst.* **59**(2) (2011) 57–64.

Helmi Abrougui is a research assistant in Mobile Robotics and Autonomous Systems Department at the Tunisian Naval Academy since 2017. In this role, he is a member of a research team, which works in research areas in relation to the control of marine and ground systems and the development of autonomous mobile robots (UGV, USV, UAV). He is a member of the Research Laboratory "Marine Technology and Naval Systems" at the Naval Academy and he published many technical papers in international journals and conferences. He received his engineering degree in Electrical Engineering and marine deck officer diploma in 2012 from the Naval Academy of Menzel Bourguiba, Tunisia. He recently received his Ph.D. degree in Electrical and Control Engineering from the Tunisian National Engineering School, Tunisia.

Samir Nejim is Professor of Control Engineering at the Naval Academy (A.N.) in Tunisia since 1991, and Head of the Research Unit Automatic Control & Marine Robotics, since its creation in 2012 at the same institution. In this role, he leads a research team, which works in research areas in relation to the automation of marine systems and the development of autonomous mobile robots. He published many technical papers in international journals and conferences, has contributed to one book and has been the supervisor of many Ph.D. and master theses. Nejim has been a PC member of many conferences and has co-edited CD-ROM proceedings of the IC_ASET international conference. He is Vice-President of the "Tunisian Association of Specialists in Electric Sciences" since 2015. He was head of university studies at the Naval Academy from 2004 to 2007. He was awarded the "Tunisian National Order of Merit in Education" in 2001. He obtained his engineering degree and a post-graduate diploma (DEA) from the "Ecole Centrale de Paris" in 1982 and 1983.